Crustal shear wave velocity structure of the western United States inferred from ambient seismic noise and earthquake data

M. P. Moschetti,[1,2] M. H. Ritzwoller,[1] F.-C. Lin,[1] and Y. Yang[1]

Received 5 February 2010; revised 11 June 2010; accepted 6 July 2010; published 8 October 2010.

[1] Surface wave dispersion measurements from ambient seismic noise and array-based measurements from teleseismic earthquakes observed with the EarthScope/USArray Transportable Array (TA) are inverted using a Monte Carlo method for a 3-D V_S model of the crust and uppermost mantle beneath the western United States. The combination of data from these methods produces exceptionally broadband dispersion information from 6 to 100 s period, which constrains shear wave velocity structures in the crust and uppermost mantle to a depth of more than 100 km. The high lateral resolution produced by the TA network and the broadbandedness of the dispersion information motivate the question of the appropriate parameterization for a 3-D model, particularly for the crustal part of the model. We show that a relatively simple model in which V_S increases monotonically with depth in the crust can fit the data well across more than 90% of the study region, except in eight discrete areas where greater crustal complexity apparently exists. The regions of greater crustal complexity are the Olympic Peninsula, the MendocinoTriple Junction, the Yakima Fold Belt, the southern Cascadia back arc, the Great Central Valley of California, the Salton Trough, the Snake River Plain, and the Wasatch Mountains. We also show that a strong Rayleigh-Love discrepancy exists across much of the western United States, which can be resolved by introducing radial anisotropy in both the mantle and notably the crust. We focus our analysis on demonstrating the existence of crustal radial anisotropy and primarily discuss the crustal part of the isotropic model that results from the radially anisotropic model by Voigt averaging. Model uncertainties from the Monte Carlo inversion are used to identify robust isotropic features in the model. The uppermost mantle beneath the western United States is principally composed of four large-scale shear wave velocity features, but lower crustal velocity structure exhibits far greater heterogeneity. We argue that these lower crustal structures are predominantly caused by interactions with the uppermost mantle, including the intrusion and underplating of mafic mantle materials and the thermal depression of wave speeds caused by conductive heating from the mantle. Upper and middle crustal wave speeds are generally correlated, and notable anomalies are inferred to result from terrane accretion at the continental margin and volcanic intrusions.

Citation: Moschetti, M. P., M. H. Ritzwoller, F.-C. Lin, and Y. Yang (2010), Crustal shear wave velocity structure of the western United States inferred from ambient seismic noise and earthquake data, *J. Geophys. Res.*, *115*, B10306, doi:10.1029/2010JB007448.

1. Introduction

[2] Although numerous seismological studies have investigated the velocity structure of the crust and upper mantle beneath the western United States on multiple spatial scales [e.g., *Grand*, 1994; *Fuis et al.*, 2001; *Shapiro and Ritzwoller*, 2002; *Tanimoto and Sheldrake*, 2002; *Gilbert and Sheehan*, 2004; *van der Lee and Frederiksen*, 2005; *Ramachandran et al.*, 2006; *Marone et al.*, 2007; *Yan and Clayton*, 2007; *Nettles and Dziewonski*, 2008], the construction of crustal velocity models over extended regions has been limited by the insensitivity or relatively poor resolution of seismological techniques to crustal structure. Surface wave inversions, for example, can constrain crustal V_S across broad regions, but crustal imaging with surface waves is generally hindered by the complexity or absence of short-period (<20 s) dispersion measurements in earthquake signals. The development of ambient noise tomography (ANT) now permits crustal imaging across large regions by enabling the measurement of short-period surface wave dispersion measurements between pairs of seismic stations. Theoretical investigations [*Snieder*, 2004; *Wapenaar*, 2004],

[1]Center for Imaging the Earth's Interior, Department of Physics, University of Colorado at Boulder, Boulder, Colorado, USA.
[2]Now at Geologic Hazards Science Center, USGS, Golden, Colorado, USA.

Copyright 2010 by the American Geophysical Union.
0148-0227/10/2010JB007448

experiments [*Lobkis and Weaver*, 2001; *Weaver and Lobkis*, 2001] and seismological applications [*Shapiro and Campillo*, 2004; *Sabra et al.*, 2005; *Shapiro et al.*, 2005] have shown that the cross-correlation of ambient seismic noise records from two seismic stations may be used to calculate the empirical Green's function (EGF), which contains information about seismic wave propagation between the stations. Surface wave dispersion measurements down to 6 s period are readily made on EGFs in the western United States [e.g., *Moschetti et al.*, 2007; *Lin et al.*, 2008] and provide strong constraints on crustal velocity structure. ANT is the inversion of interstation dispersion measurements obtained from the EGFs to construct surface wave dispersion maps and has already been used to produce dispersion maps across various regions around the globe and at multiple scales [e.g., *Yao et al.*, 2006; *Brenguier et al.*, 2007; *Cho et al.*, 2007; *Lin et al.*, 2007; *Villaseñor et al.*, 2007; *Yang et al.*, 2007; *Bensen et al.*, 2008; *Yang et al.*, 2008a; *Zheng et al.*, 2008]. Determination of the seismic velocity structure beneath the western United States benefits from the application of novel observational techniques to data from the EarthScope/USArray Transportable Array (TA). As the TA moves across the United States, about 400 stations on a nearly uniform 70 km grid record continuous data simultaneously. Each seismic station collects data for about two years before it is re-deployed to a new location. The station density and spatial coverage of the TA span the resolution gap between regional [e.g., *Tanimoto and Sheldrake* 2002] and global scale [e.g., *van der Lee and Frederiksen*, 2005; *Shapiro and Ritzwoller*, 2002] studies. Detailed images of the crust and upper mantle in the western United States have begun to emerge [e.g., *Gilbert and Fouch*, 2007; *Burdick et al.*, 2008; *Pollitz*, 2008; *Yang et al.*, 2008b; *West et al.*, 2009].

[3] In this study, we apply ANT together with multiple plane wave earthquake tomography (MPWT) [*Yang et al.*, 2008b] to data from the TA. Application of ANT to the TA data provides Rayleigh wave group [*Moschetti et al.*, 2007] and Rayleigh and Love wave phase speed [*Lin et al.*, 2008] maps, which are strongly sensitive to the crust and uppermost mantle and cover the entire western United States. MPWT likewise benefits from the high station density and broad spatial coverage of the TA. MPWT is an extension of the two-plane wave method of *Forsyth and Li* [2005] in which complexities in the incoming wavefield are fit with two plane waves. While two plane waves are sufficient to characterize the incoming wavefield for relatively small arrays, for regions the size of the western United States additional plane waves are needed to model the incoming wavefield from each earthquake. MPWT provides Rayleigh wave phase speed estimates across the western United States that are at about the same resolution and are readily inverted together with the dispersion measurements from ANT [*Yang et al.*, 2008b].

[4] It is common practice in seismology to invert dispersion maps from earthquake measurements [*Shapiro and Ritzwoller*, 2002] or ANT [*Cho et al.*, 2007; *Bensen et al.*, 2009; *Stehly et al.*, 2009], as well as to use them jointly [*Yao et al.*, 2008; *Yang et al.*, 2008a, 2008b], to infer the 3-D V_S structure of the crust and upper mantle. Notably, *Bensen et al.* [2009] carried out an inversion of Rayleigh and Love wave dispersion measurements obtained from ANT for V_S structure across the entire United States. However, this work was completed before the TA was deployed in the western United States and the corresponding resolution is lower than what now can be achieved. *Yang et al.* [2008b] inverted Rayleigh wave phase speed measurements from ANT and MPWT for a V_{SV} model of the crust and upper mantle in the western United States, but this study did not include Love waves and the model did not account for the crustal and uppermost mantle radial anisotropy ($V_{SH} \neq V_{SV}$) that has been documented, for example, by *Nettles and Dziewonski* [2008], *Bensen et al.* [2009], and *Moschetti et al.* [2010]. Inversions of Rayleigh wave data alone cannot untangle shear wave velocity perturbations caused by radial anisotropy from those caused by isotropic wave speed anomalies. In addition to Love and Rayleigh wave phase speed measurements, we incorporate here Rayleigh wave group speed data from ANT. Group speed measurements have shallower depth sensitivity than phase speed measurements at the same period and provide additional constraints on crustal velocity structure.

[5] We seek here, in particular, to identify a single parameterization, particularly of the crust, that can be applied across the entire western United States except perhaps at isolated locations of greater complexity. We document how across most of the western United States crustal wave speeds can be considered to increase monotonically with depth (thus crustal low-velocity zones generally are not required by the data), but crustal and upper mantle radial anisotropy is needed to fit Rayleigh and Love wave dispersion data simultaneously. Our discussion is focused, however, on the isotropic component of the 3-D radially anisotropic V_S model. The isotropic model presented here is constructed by Voigt averaging the V_{SH} and V_{SV} models that result from the radially anisotropic inversion. Discussion and interpretation of the radial anisotropy is the subject of *Moschetti et al.* [2010].

2. Methods

[6] The inversion of surface wave dispersion measurements for a 3-D V_S model is carried out in two steps. The first step, termed surface wave tomography, is the inversion for Rayleigh and Love wave dispersion maps. This step is described by *Moschetti et al.* [2007], *Lin et al.* [2008], and *Yang et al.* [2008b]. The second step, which we carry out here, is inversion of the surface wave dispersion maps for a 3-D V_S model. Here, we use a Monte Carlo method to infer a radially anisotropic V_S model of the crust and uppermost mantle beneath the western United States, referred to as model m_1. We calculate the isotropic component of this model by Voigt averaging. For comparison, we also carry out the direct inversion for an isotropic model called m_0. Because we employ a Monte Carlo inversion scheme, the V_S structure beneath each grid point is represented by a set of models that fit the data similarly well, which provides uncertainty estimates used to identify robust model features.

2.1. Surface Wave Tomography and Construction of Local Dispersion Curves

[7] Surface wave dispersion measurements from ANT and MPWT are combined because the joint period band is broader than the individual bands. ANT provides short- to

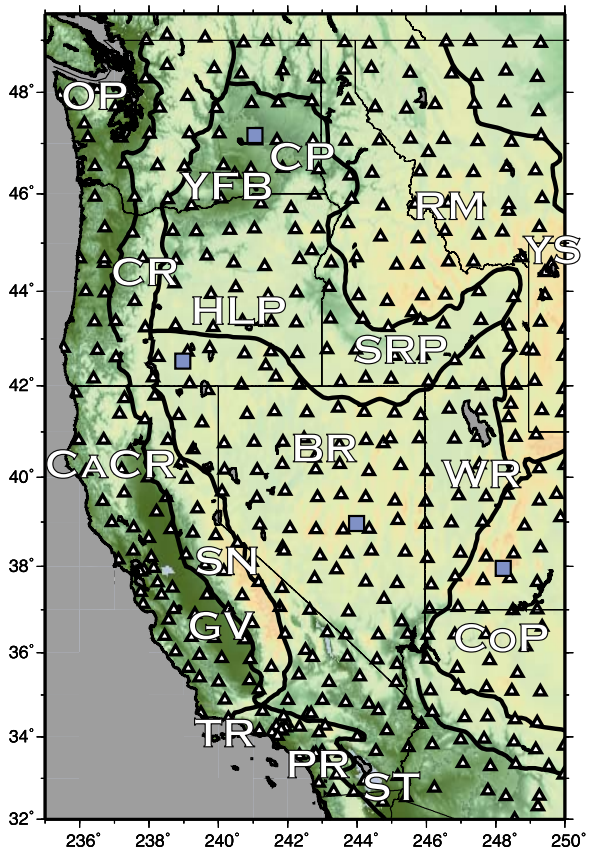

Figure 1. Western United States inversion area, showing Transportable Array (TA) and other stations utilized in this study. Major physiographic regions are outlined with bold black lines. Geologic and tectonic features in the region include the Basin and Range (BR),California Coast Ranges (CaCR), Cascade Range (CR), Colorado Plateau (CoP), Columbia Plateau (CP), Great Central Valley (GV), High Lava Plains (HLP), Olympic Peninsula (OP), Peninsular Range (PR), Rocky Mountains (RM), Salton Trough (ST), Sierra Nevada (SN), Snake River Plain (SRP), Transverse Range (TR), Wasatch Range (WR), Yakima Fold Belt (YFB), and Yellowstone (YS). The grid point locations for coordinates (239.0,42.5), (241.0,47.0), (248.0,38.0), and (244.0, 39.0), discussed in Figures 6–9, are plotted with blue squares.

intermediate-period measurements (6–40 s) and MPWT provides intermediate- to long-period measurements (25–100 s). The combined dispersion curve at each location has strong sensitivity to both the crust and upper mantle. The dispersion maps and measurements of *Moschetti et al.* [2007], *Yang et al.* [2008b] and *Lin et al.* [2008] are extended spatially in this study. We briefly summarize these methods here.

2.1.1. Surface Wave Tomography

[8] Ambient noise data processing entails station record pre-processing (filtering, time and frequency domain normalization), cross correlation of station records to produce empirical EGFs, selection of EGFs, measurement of group and phase speeds, and inversion of the group and phase speed measurements at each period for dispersion maps. The methods described by *Bensen et al.* [2007] and *Lin et al.* [2008] are followed here. By cross-correlating seismic records observed at 526 stations between October 2004 and December 2007, more than 128,000 EGFs are calculated. Most of the waveform data is taken from TA stations, but additional data from regional networks is also incorporated. Figure 1 presents the major physiographic provinces and the locations of seismic stations used in this study. Because of the evolving nature of the TA, not all of the stations operate concurrently. The resulting time series range from six months to more than three years in duration. Linear tomographic inversions of the interstation Rayleigh wave group and phase speeds and the Love wave phase speeds are carried out using Gaussian-shaped sensitivity kernels centered on the great circle path between stations [*Barmin et al.*, 2001]. The Rayleigh and Love wave dispersion maps that result are in period bands of 6–40 and 8–32 s, respectively. Because of the large uncertainties associated with the Love wave group speeds, we do not incorporate these data in the inversion for V_S structure. We invert the Rayleigh wave phase and group speeds with the Love wave phase speeds for shear wave velocity structure beneath the western United States.

[9] The ANT-derived dispersion maps are updated and expanded from the Rayleigh wave group speed maps presented by *Moschetti et al.* [2007] and the Rayleigh and Love wave phase speed maps of *Lin et al.* [2008]. The measurement of Rayleigh wave phase speeds from teleseismic earthquakes using MPWT follows the methods of *Yang et al.* [2008b] employing 250 earthquakes recorded by the TA between January 2006 and September 2008. Twelve independent plane waves are used to model the incoming wavefield at the TA for each earthquake. Rayleigh wave phase speed maps from MPWT are generated in the 25–100 s period band.

2.1.2. Local Dispersion Curves

[10] The local dispersion curves are generated from the surface wave dispersion maps by selecting the group and phase speeds at each point on a 0.5° by 0.5° grid as a function of period. Separate local dispersion curves are constructed from the dispersion maps obtained from ANT and MPWT. In the period band of overlap of the methods (25–40 s), *Yang et al.* [2008b] demonstrated substantial agreement between the Rayleigh wave phase estimates. The mean absolute difference between the MPWT and ANT phase speed estimates in the 25–40 s period band is about 15 m/s, which, as discussed below, is within a standard deviation of the dispersion measurements. We follow *Yang et al.* [2008b] by averaging measurements in the overlapping period band to produce combined Rayleigh wave phase speed curves with a period band of 6–100 s. These dispersion curves are sensitive to both crustal and upper mantle velocity structures. Examples of the local dispersion curves are plotted in Figure 2 and present some of the variation observed between the group and phase speeds from different regions. Although the focus of this study is the crustal structure of the western United States, and dispersion measurements from ANT provide the strongest constraints at this depth, the incorporation of the MPWT measurements reduces the trade-off in shear wave velocities across the Moho and provides improved constraints on upper mantle

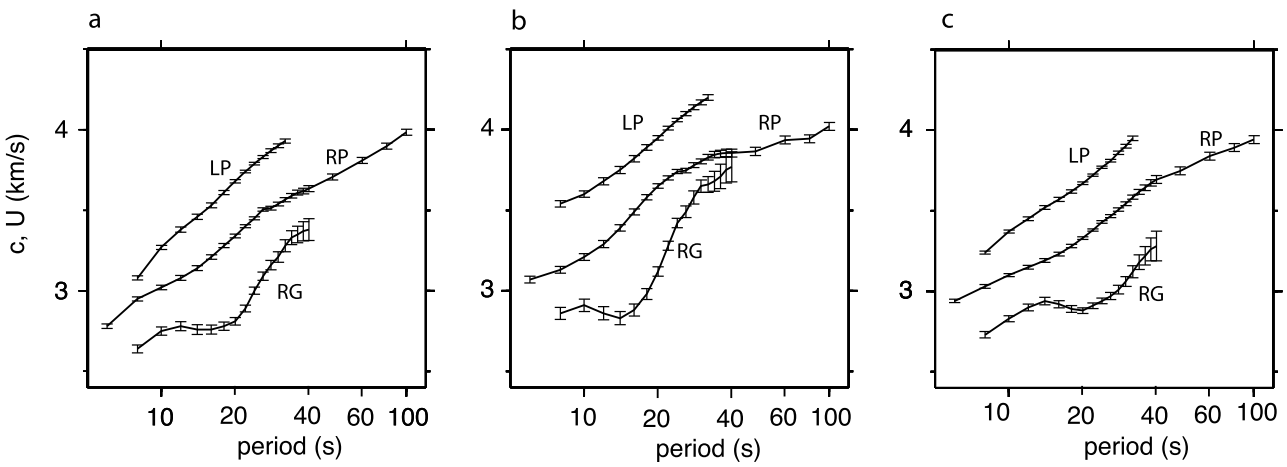

Figure 2. Dispersion curves and associated uncertainty values from (a) the southern Cascadia back arc (239.0,42.5), (b) the Yakima Fold Belt (241.0,47.0), and (c) the Colorado Plateau (248.0,38.0). Locations of these grid points are identified in Figure 1. RP, RG, and LP refer to the Rayleigh wave phase and group speeds and Love wave phase speeds, respectively.

velocity structure. Love wave measurements have not yet been obtained with MPWT, so they derive entirely from ANT between 8 and 32 s period. Love wave constraints on mantle structure, therefore, are much weaker than from Rayleigh waves.

2.1.3. Data Uncertainties

[11] We require uncertainty estimates for the local dispersion curves taken from the dispersion maps in order to assess the fit of model-predicted dispersion curves and to weight data in the inversion. Estimates of uncertainties in the interstation ambient noise dispersion measurements are obtained in a straightforward way by temporal subsetting [e.g., *Bensen et al.*, 2007]. Estimates of local uncertainties for the dispersion maps are not as straightforward, although uncertainties in the Rayleigh wave phase speeds from ambient seismic noise are now directly calculated by Eikonal tomography [*Lin et al.*, 2009]. To estimate uncertainties in local Rayleigh wave group and Love wave phase dispersion curves we simply scale the Rayleigh wave phase uncertainties by the relative errors in the interstation ambient noise dispersion measurements. Specifically, uncertainties in ambient noise dispersion measurements are determined in two steps. (1) We estimate the ratios of the measurement uncertainties of the Rayleigh wave group and Love wave phase speeds compared to the Rayleigh wave phase speeds (i.e., $\sigma^{RG}(T)/\sigma^{RP}(T)$ and $\sigma^{LP}(T)/\sigma^{RP}(T)$) from the temporal variability in the observed EGFs. *RP*, *RG* and *LP* refer to Rayleigh wave phase and group speed and Love wave phase speed, respectively, and T is the period of the measurement. To calculate the temporal variations in the Rayleigh and Love wave interstation dispersion measurements, we use 34 and 21 six month time windows, respectively. These uncertainty ratios, averaged over the study region, are plotted in Figure 3a. (2) We then use the uncertainty ratios of the measured data to scale the Rayleigh wave phase speed uncertainties ($\tilde{\sigma}_i^{RP}$) determined from Eikonal tomography. Examples of the Rayleigh wave phase speed uncertainties from Eikonal tomography, at several periods, are presented in Figure 4. Equations (1) and (2) are used to estimate uncertainty values for the Rayleigh wave group speed and Love wave phase speed at each grid point, i,

$$\tilde{\sigma}_i^{RG}(T) = \frac{\sigma^{RG}(T)}{\sigma^{RP}(T)}\tilde{\sigma}_i^{RP}(T) \tag{1}$$

$$\tilde{\sigma}_i^{LP}(T) = \frac{\sigma^{LP}(T)}{\sigma^{RP}(T)}\tilde{\sigma}_i^{RP}(T) \tag{2}$$

Averages across the study region of the local uncertainties in the dispersion curves from the ambient noise are presented in Figure 3b. Spatially and frequency-averaged uncertainties in the Rayleigh wave phase and group speed and Love wave phase speed are 14.5, 36.8, and 13.4 m/s, respectively. Examples of the uncertainty values in the Rayleigh wave phase and group speeds and Love wave phase speeds from three geographic grid points are plotted as error bars in the dispersion curves of Figure 2.

[12] Uncertainties in the Rayleigh wave phase speed maps derived from MPWT follow the method of *Yang et al.* [2008b] in which estimates are calculated from the inversion residuals. Uncertainty values are plotted as a function of period in Figure 3c and show a mean uncertainty value of 27.6 m/s. On average, Rayleigh wave phase speed uncertainty from MPWT is estimated to be about twice the phase speed uncertainties from ambient noise, but less than the ambient noise group speed errors.

2.2. Inversion of Local Dispersion Curves for a 3-D V_S Model

[13] The data for the V_S inversion are the local Rayleigh and Love wave dispersion curves generated on a 0.5° by 0.5° grid across the study region. At each grid point we use a Monte Carlo method to sample parameter space for many trial models and assess the misfit of the corresponding

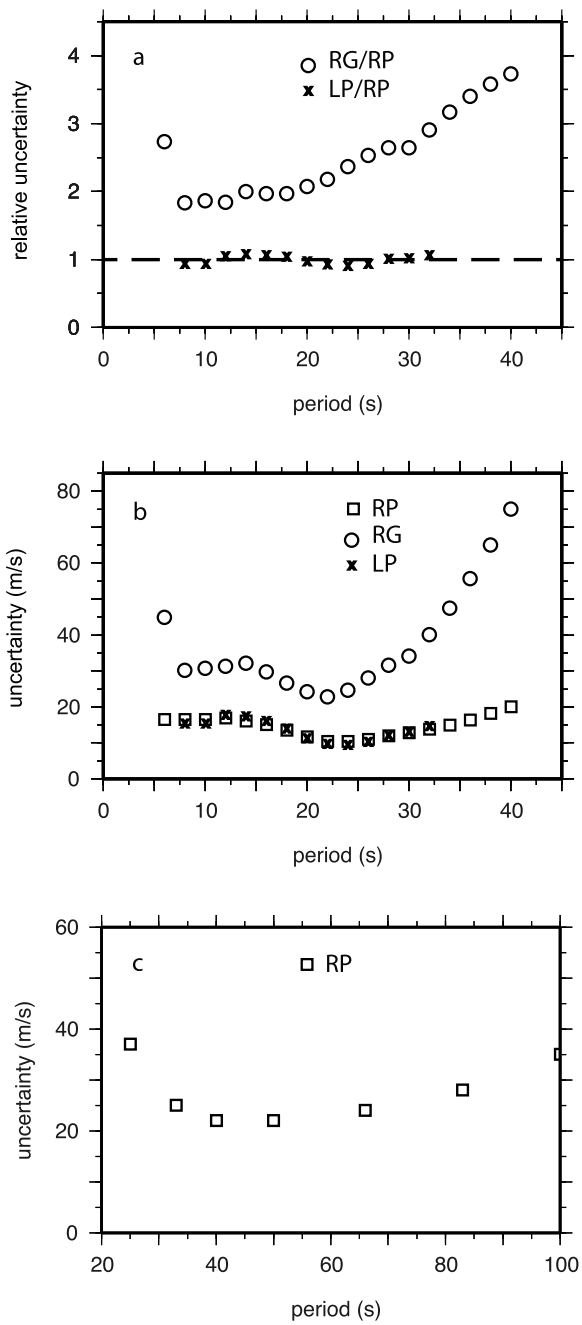

Figure 3. Uncertainties in Rayleigh wave phase and group and Love wave phase speeds. (a) Estimates of the ratios of uncertainties determined from the temporal variation in the interstation dispersion measurements averaged over all measurements. Circles and crosses represent the ratios $\sigma^{RG}(T)/\sigma^{RP}(T)$ and $\sigma^{LP}(T)/\sigma^{RP}(T)$, respectively. *RP*, *RG*, and *LP* refer to the Rayleigh wave phase and group and Love wave phase speeds, respectively. (b) Spatially averaged Rayleigh wave phase and group speed uncertainties are plotted with squares and circles, respectively. The Love wave phase speed uncertainties are plotted with crosses. Mean uncertainty values for the Rayleigh wave phase and group speed and Love wave phase speed are 14.5, 36.8, and 13.4 m/s, respectively. (c) Rayleigh wave phase speed uncertainties from MPWT. Mean uncertainty is 27.6 km/s.

predicted dispersion curves to the dispersion data. All models with corresponding data misfits less than a misfit threshold value are accepted and form the set of "acceptable models" at that grid point. This general inversion procedure has been used previously to construct regional and global scale V_S models [*Shapiro and Ritzwoller*, 2002; *Yang et al.*, 2008a; *Bensen et al.*, 2009]. From the set of accepted models at each grid point, we calculate the mean and standard deviation to represent the velocity structure and uncertainty as a function of depth.

[14] For the purpose of comparison, we invert the local dispersion curves for two models. (1) We first invert the Rayleigh and Love wave data for an initial isotropic ($V_{SH} = V_{SV}$) model, m_0. This inversion also defines a restricted parameter space for each grid point to be used in the construction of the second model. (2) As discussed below, the

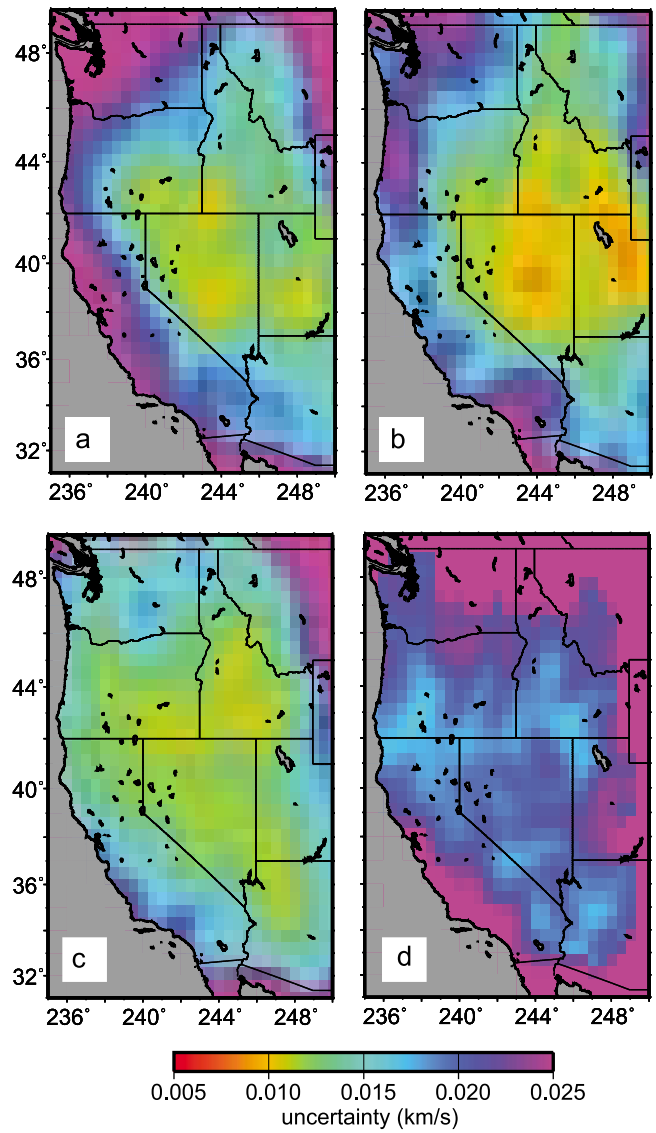

Figure 4. Rayleigh wave phase speed uncertainties for ANT are taken from the Eikonal tomography uncertainty estimates of *Lin et al.* [2009]. Examples are plotted at (a) 8, (b) 16, (c) 30, and (d) 40 s periods.

isotropic model m_0 systematically misfits the data, which we call the Rayleigh-Love discrepancy. Thus, we reinvert the Rayleigh and Love wave data for a radially anisotropic model ($V_{SH} \neq V_{SV}$) by searching the restricted parameter space in the vicinity of the initial model, m_0. We compute the final model, m_1, from the Voigt average velocities of the set of accepted V_{SH} and V_{SV} models.

2.2.1. Model Parameterization and A priori Constraints

[15] One of the principal goals of this study is to determine whether a single, simple parameterization can be found to fit the Rayleigh and Love wave data across the entire United States. Because seismic noise cross-correlation techniques facilitate the measurement of surface wave dispersion at shorter periods (<15 s) than have been used in most previous surface wave inversions for shear wave velocity structure [e.g., *Shapiro and Ritzwoller*, 2002], and because of the evidence for crustal radial anisotropy, we investigate the use of a simple model parameterization to explain these novel observations. For this reason, the model parameterization is uniform across the study region. From earlier experience [e.g., *Bensen et al.*, 2009; *Yang et al.*, 2008a], we know that some model complexity is needed to fit broadband dispersion data. There needs to be a well defined sedimentary layer, several crystalline layers in the crust, significant topography on the Moho, smooth vertical variation in the mantle, and the imposition of a priori information on sedimentary and crustal thicknesses at least. For this reason, the crustal model comprises a sediment layer underlain by three crystalline crustal layers. The layer thickness ratio for the three crystalline crustal layers is 1:2:2, where the shallowest layer is thinnest. Mantle V_S structure is modeled from the Moho to 250 km depth with five cubic B splines. Below 250 km, the models tie into the V_S model of *Shapiro and Ritzwoller* [2002]. Where required, water layer depths are constrained by data from the NOAA GEODAS database [*NGDC*, 2009]. In Step 1 of the inversion, we invert for m_0 comprising thirteen independent variables: sediment thickness, crustal thickness, V_S in each crustal layer, V_P/V_S in the sedimentary layer and in the crystalline crust, and five cubic B spline coefficients (for mantle V_S structure). This inversion is discussed further in section 2.2.2. In Step 2, the inverted variables also include V_{SH} and V_{SV} separately in the middle and lower crustal layers and in the uppermost mantle. Radial anisotropy is allowed only in the middle and lower crust and upper mantle. Sensitivity tests find that upper crustal radial anisotropy cannot resolve the Rayleigh-Love discrepancy [*Moschetti et al.*, 2010]. This inversion produces model m_1, which is discussed in detail in section 2.2.3.

[16] A radially anisotropic medium is represented by five parameters; for example, the Love parameters A, C, F, L, and N [*Love*, 1927]. Because surface waves are primarily sensitive to V_{SH} and V_{SV}, which are related to the N and L parameters, respectively, in Step 2 we directly invert for only these parameters and set the remaining parameters to fixed values or determine their values from scaling relationships. We fix the nondimensional parameters $\phi = C/A = (V_{PV}/V_{PH})^2$, and $\eta = F/(A - 2L)$ at unit amplitude, which are their values for an isotropic medium.

[17] In both of the inverted models, density structure is calculated below each grid point using an empirical relation between wave speed and density [*Brocher*, 2005]. The Q model is taken from PREM. Sensitivity tests indicate that reasonable variations in these assumptions have little effect on the strength of the resulting radial anisotropy in the model either because the expected perturbations are small or because perturbations cause both the Rayleigh and Love wave speeds to increase or decrease together and cannot, therefore, resolve the crustal Rayleigh-Love discrepancy, as discussed in further by *Moschetti et al.* [2010].

[18] A 13–15 parameter model such as we construct beneath each grid point is somewhat complicated. It should be understood, however, that because the inversion procedure is a model-space sampling method, the introduction of each extra parameter is met with greater variability (and hence uncertainty) in the other variables determined in the inversion. In order to guarantee physically reasonable models, it is important to impose a priori constraints on the parameter space searched in the inversion. We impose constraints on P and S wave speeds as well as sediment and crustal thicknesses. The range of values for V_S and V_P/V_S in the crust and upper mantle is based on previous studies [*Christensen and Mooney*, 1995; *Shapiro and Ritzwoller*, 2002; *Brocher*, 2005]. Because surface waves have little sensitivity to vertical velocity discontinuities, such as the Moho, sediment and crustal thickness constraints are needed to stabilize the velocity structure. Sediment thicknesses are taken from the Global Sediment Model of *Laske and Masters* [1997] but we allow perturbations of up to 250 m. Crustal thickness constraints derive from the receiver function estimates and attendant uncertainties of *Gilbert and Fouch* [2007], where the mean uncertainty in crustal thickness is about 5 km. Model parameterization and constraints are summarized in Figure 5 and Tables 1 and 2.

[19] An additional important constraint is the requirement that crustal velocities increase monotonically with depth, so that we seek models without a crustal low-velocity zone. Crustal low-velocity zones actually are expected in some regions, and we point to evidence later that some regions of poor data fit may be improved by relaxing this constraint.

2.2.2. Inversion for the Initial Isotropic 3D Model, m_0

[20] Inversion of the local dispersion curves for the initial isotropic model, m_0, is carried out using the Neighborhood Algorithm [*Sambridge*, 1999], and surface wave dispersion curves are calculated using the *Computer Programs in Seismology* package [*Herrmann and Ammon*, 2004]. For an isotropic model, these dispersion curves are verified to be consistent with those from the code MINEOS [*Masters et al.*, 2007]. Each trial model is used to calculate the corresponding Rayleigh wave phase and group and Love wave phase speeds.

[21] The fit of the model-predicted dispersion curves to the local dispersion curves is assessed with the reduced chi squared misfit parameter, which we refer to as "chi squared," χ^2:

$$\chi^2 = \frac{1}{n}\sum_{i=1}^{n}\frac{(d_i - p_i)^2}{\sigma_i^2}, \tag{3}$$

where n is the total number of discrete periods along the three dispersion curves, d_i and p_i are the observed and model-predicted dispersion values, and σ_i are the data uncertainty values associated with each measurement, as

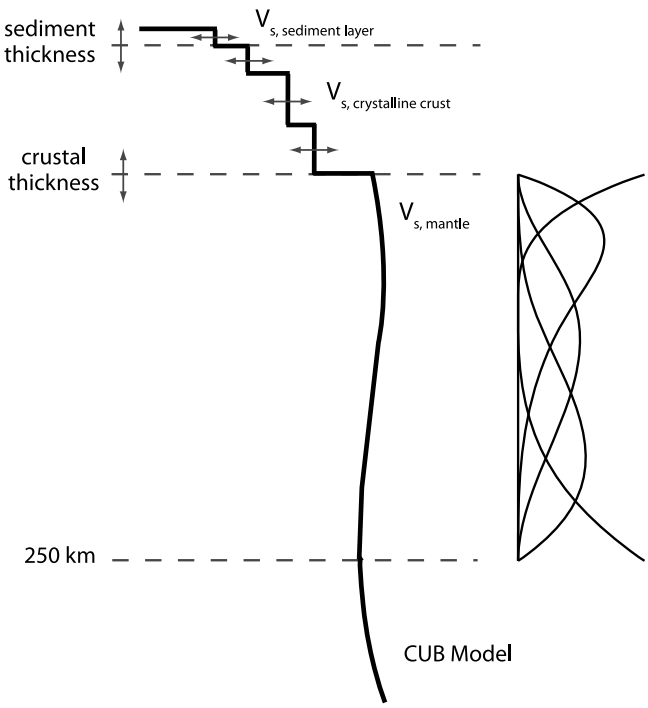

Figure 5. Depiction of the model parameterization. The models m_0 and m_1 are parameterized with four crustal layers and five cubic B splines in the mantle to 250 km depth. Crustal layers include a sedimentary layer and three crystalline layers. The thickness ratio of the crystalline crustal layers is fixed at 1:2:2. Sediment and crustal thickness perturbations are allowed. Crustal velocities are required to increase monotonically with depth. Below 250 km depth, the model ties into the V_S model of *Shapiro and Ritzwoller* [2002]. Model m_1 includes radial anisotropy ($V_{SH} \neq V_{SV}$) in the middle and lower crust and in the upper mantle (not shown).

described in section 2.1.3. We set the threshold for accepting models at two units greater than the value of the best fitting model, $\chi^2_{\min}$:

$$\chi^2_{thresh} = \chi^2_{\min} + 2. \quad (4)$$

Only trial models with corresponding χ^2 values below the threshold value are accepted. The initial isotropic model, m_0, is the mean of the set of accepted models and its uncertainty is the standard deviation of the accepted models at each depth.

2.2.3. Inversion for the Radially Anisotropic Model, m_1

[22] To construct the second model, we restrict the parameter space at each grid point to the parameter space defined by the set of accepted models from the isotropic model, m_0. Where the peak-to-peak perturbation of any parameter is less than 10%, the parameter range is set to a ± 5% perturbation to the isotropic model, m_0. On average, the restricted parameter space for each variable encompasses 65% of the parameter space allowed in the inversion for the initial model, m_0, and is sufficiently large to encompass the structural perturbations needed to fit the data and characterize the trade-offs between different model parameters.

[23] We follow the approach discussed by *Moschetti et al.* [2010] to invert for crustal and mantle radial anisotropy. Crustal anisotropy is introduced to the middle and lower crystalline crustal layers with equal amplitudes ($2|V_{SH}-V_{SV}|/(V_{SH}+V_{SV})$). Because the period band of the Rayleigh wave phase speed measurements extends to 100 s period, these measurements constrain V_{SV} to depths greater than 250 km. However, the Love wave phase speed data used in this inversion have little sensitivity to mantle structures below 60 km depth, and we cannot reasonably constrain V_{SH} below this depth. Although in most other radially anisotropic V_S models the amplitude of radial anisotropy in the upper mantle decreases with depth [*Dziewonski and Anderson*, 1981; *Shapiro and Ritzwoller*, 2002; *Nettles and Dziewonski*, 2008], in our inversion mantle radial anisotropy is represented with a single amplitude from the Moho to 250 km depth. If a PREM type [*Dziewonski and Anderson*, 1981] mantle anisotropy profile (where the amplitude of radial anisotropy is maximum immediately below the Moho and decreases to zero at 220 km) were to exist in the Earth, our parameterization would overestimate V_{SH}, except in the uppermost mantle. For the amplitudes of mantle anisotropy observed in this model, errors in V_{SH} caused by our parameterization would produce less than a 0.5% V_S perturbation above 60 km depth.

[24] Trial models are selected in the inversion by uniform Monte Carlo sampling of the restricted parameter space. The program MINEOS [*Masters et al.*, 2007] is used to calculate the surface wave dispersion curves because it accurately accounts for radial anisotropy in the Earth. However, the calculation of dispersion curves by MINEOS is significantly slower than the calculations for the initial isotropic model, m_0 [*Herrmann and Ammon*, 2004]. To accelerate the inversion, we follow *Shapiro and Ritzwoller* [2002] and

Table 1. Model Parameter Constraints for the Isotropic Initial Model m_0

Model Parameter	Range	Source
Sediment thickness	±250 m	*Laske and Masters* [1997]
Crustal thickness	±5 km	*Gilbert and Fouch* [2007]
Layer thickness ratio, crystalline crust	1:2:2	
V_S, sediments	1.5–3.0 km/s	*Christensen and Mooney* [1995] and *Brocher* [2005]
V_S, upper crust	2.0–3.5 km/s	*Christensen and Mooney* [1995] and *Brocher* [2005]
V_S, middle and lower crust	2.5–4.0 km/s	*Christensen and Mooney* [1995] and *Brocher* [2005]
V_P/V_S, sediment layer	1.75–2.5 km/s	*Brocher* [2005]
V_P/V_S, crystalline crust (same in all layers)	1.70–1.8 km/s	*Brocher* [2005]
V_P/V_S, mantle	1.8 km/s	*Shapiro and Ritzwoller* [2002]
V_S, upper mantle	3.7–4.75 km/s	*Shapiro and Ritzwoller* [2002]

Table 2. Model Parameter Constraints for the Radially Anisotropic Model m_1

Model Parameter	Minimum Range	Source
Sediment thickness	±250 m	*Laske and Masters* [1997]
Crustal thickness	±5 km	*Gilbert and Fouch* [2007]
Layer thickness ratio, crystalline crust	1:2:2	
V_S, sediments	[a]	
V_S, upper crust	[a]	
V_S, middle crust	[a]	
V_S, lower crust	[a]	
V_P/V_S, sediment layer	[a]	
V_P/V_S, crystalline crust	[a]	
V_P/V_S, mantle	[a]	
V_S, upper mantle	[a]	
Radial anisotropy, sediment and upper crust	0%	*Moschetti et al.* [2010]
Radial anisotropy, middle and lower crust	Unconstrained	*Moschetti et al.* [2010]
Radial anisotropy, upper mantle	≤10%	*Nettles and Dziewonski* [2008]

[a]At least ± 5% from model m_0.

employ the method of *James and Ritzwoller* [1999]. At each grid point, 500,000 trial models are sampled from the restricted parameter space. As in the inversion for the initial model, we set the χ^2 threshold for model acceptance at two units greater than the χ^2 value of the best fitting model. Where the accepted set comprises fewer than 1000 models, we continue forward modeling until 1000 models are accepted. Accepted models define the set of models for m_1. The model space of each variable from the set of final models, on average, encompasses about 57% of the full parameter space allowed in the inversion for the initial model, m_0. Where the parameter space in the set of final models is not significantly different from the space allowed for the initial inversion (i.e., the model space described by Table 1), we find that those parameters are either poorly sensitive to model perturbations and have high corresponding model uncertainties, or strong parameter trade-offs exist within the model.

2.2.4. Effect of Model Constraints on the Final Set of Accepted Models

[25] The most important effect of the application of model constraints is the imposition of an a priori understanding of the Earth. By reducing the allowed model space in the inversion, constraints determine which models are physically plausible. To ensure that the model space search is not too restricted, which would result in the inversion disallowing physically plausible models, we define the model constraints based on observed and estimated parameter ranges of P and S wave speeds, crustal and sediment thicknesses, and strength of radial anisotropy [*Christensen and Mooney*, 1995; *Laske and Masters*, 1997; *Shapiro and Ritzwoller*, 2002; *Brocher*, 2005; *Gilbert and Fouch*, 2007; *Nettles and Dziewonski*, 2008]. Model constraints have the greatest effect on the final model where the inversion is not stabilized or where trade-offs in the model parameters exist and the application of model constraints guides selection of trial models. Two examples of the effects of model constraints on the parameter trade-offs in the inversion are presented here.

[26] 1. Crustal thickness and lower crustal V_S trade off. An example is in central Nevada (grid point (244.0,39.0)), presented in Figure 6. At this grid point, crustal thickness and lower crustal V_S in the set of accepted models range over about 10 km and 0.5 km/s, respectively. The insensitivity of the dispersion data to crustal thickness is evidenced by the relatively uniform distribution of values.

[27] 2. Crustal V_P and the strength of crustal radial anisotropy trade off. We find, however, that in the absence of radial anisotropy in the crust, implausible crustal V_P values are required to reduce data misfit. This trade-off is well known and has previously been documented for mantle radial anisotropy [e.g., *Shapiro and Ritzwoller*, 2002]. Figure 7 presents the results from two inversions for a grid point in central Nevada (244.0,39.0): one where the model is parameterized as model m_1, described in Table 2 (Figure 7a), and one where radial anisotropy is not allowed in the crust but V_P/V_S values are allowed to range between 1.5 and 2.0 (Figure 7b). Although the inversion results of Figure 7b show that radial anisotropy is not formally required in the

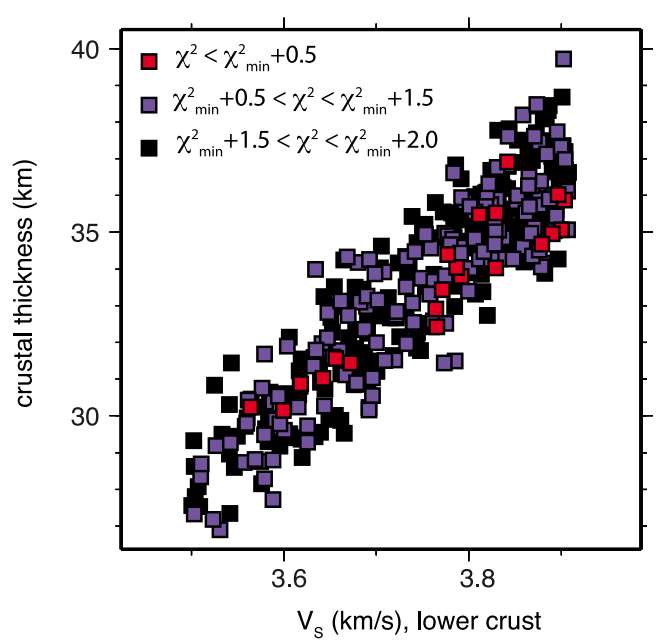

Figure 6. Trade-off between lower crustal V_S and crustal thickness for a point in central Nevada (244.0,39.0) from model m_1. Crustal thicknesses range over more than 10 km and lower crustal V_S ranges over 0.5 km/s in the set of accepted models.

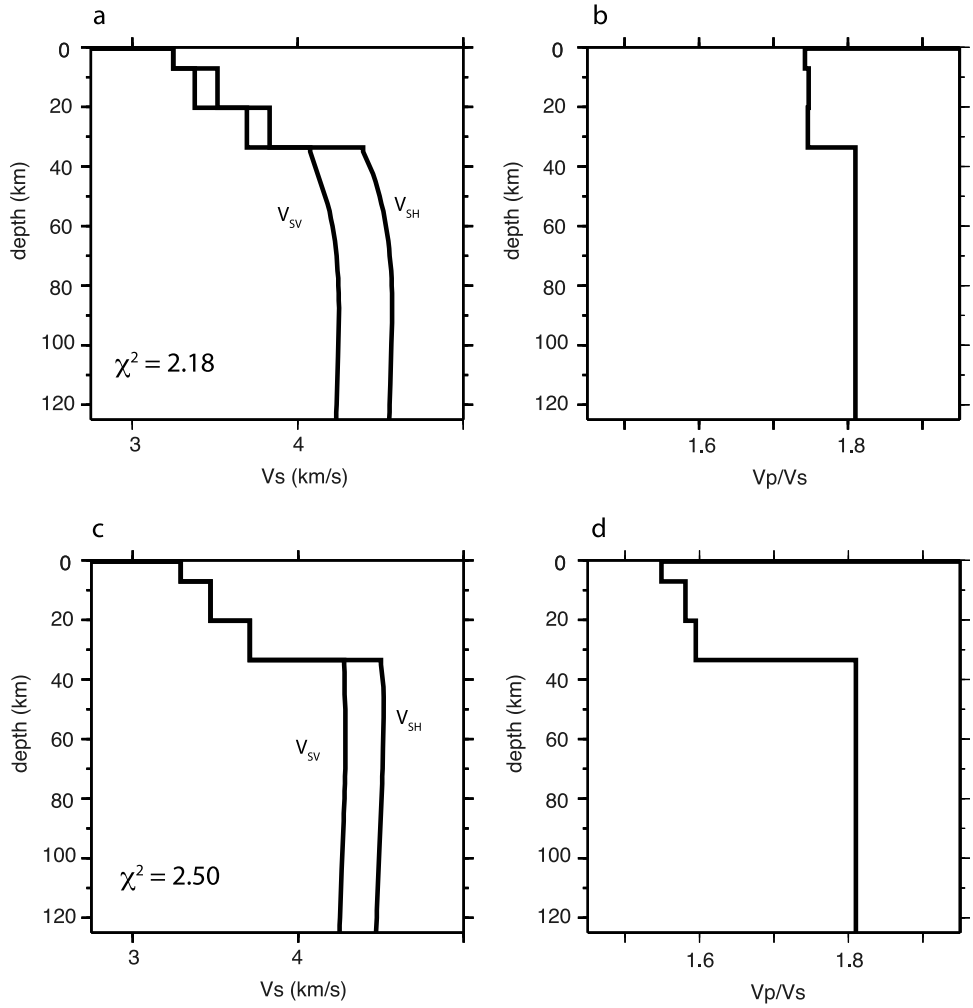

Figure 7. Effect of V_P/V_S on the strength of radial anisotropy in the crust at a location in central Nevada (244.0,39.0). (a) V_S and (b) V_P/V_S models that result from an inversion where the model includes radial anisotropy in the crust and upper mantle and is subjected to the constraints described in Table 2. (c) V_S and (d) V_P/V_S models that result from an inversion where V_P/V_S values are allowed to range between 1.5 and 2.0 in the crystalline crust and the crust is isotropic. There is a strong trade-off between crustal V_P/V_S and the strength of radial anisotropy in the crust, but V_P/V_S values less than 1.6 are generally considered to be physically implausible across large regions and are in conflict with other studies [e.g., *Gilbert and Sheehan*, 2004].

crust, V_P values in the crust range from 5.0 to 5.4 km/s and corresponding V_P/V_S values range from 1.54 in the upper crust to 1.59 in the lower crust. Previous studies indicate that these values of V_P and V_P/V_S are too low to be physically plausible [e.g., *Benz et al.*, 1990; *Gilbert and Sheehan*, 2004]. Our preferred inversion result is one where V_P/V_S is constrained by the values of Tables 1 and 2 and radial anisotropy is allowed in the middle and lower crust and in the uppermost mantle. The imposition of physically defined constraints on V_P/V_S reduces the trade-offs among these parameters and guides the selection of trial models that are used to construct the final model, m_1.

3. Three-Dimensional Inversion Results

3.1. Construction of the V_S Profiles

[28] Inversion of the local dispersion curves produces a set of 1-D V_{SH} and V_{SV} profiles at each grid point on a 0.5° by 0.5° grid across the western United States. An example of the data fit and of the accepted models from central Nevada (244.0,39.0) is presented in Figure 8.

[29] An isotropic V_S model is calculated from V_{SH} and V_{SV} by a Voigt average for the case of small anisotropy [*Babuska and Cara*, 1991; *Panning and Romanowicz*, 2006]:

$$V_S = \left(\frac{V_{SH}^2 + 2V_{SV}^2}{3}\right)^{1/2} \tag{5}$$

Isotropic V_S models at each grid point are defined by the set

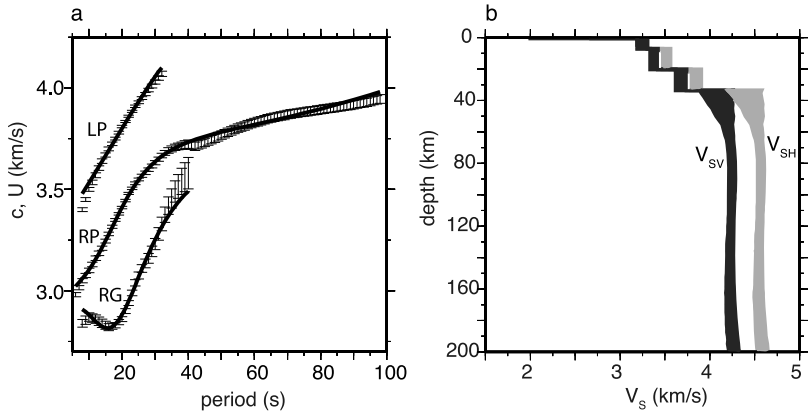

Figure 8. Inversion results from central Nevada (244.0,39.0). (a) Dispersion curve fit to the observed local dispersion values presented as error bars. The dispersion curves for the best fitting model are plotted with solid black lines. (b) The corridor of accepted V_{SH} and V_{SV} models are plotted in light and dark gray, respectively. RP, RG, and LP refer to Rayleigh wave phase and group speed and Love wave phase speed, respectively.

of models calculated from all accepted V_{SH} and V_{SV} profiles. We represent isotropic V_S at each grid point by the middle of the corridor of accepted models, and model uncertainties are presented as the standard deviations of the set of accepted isotropic models about this mean. Isotropic V_S profiles from points in three tectonic provinces are given in Figure 9 to provide examples of the variations in velocity structure and uncertainty observed across the region.

3.2. V_S Model, Uncertainties, and the Identification of Persistent Model Features

[30] The final 3-D isotropic V_S model comprises the mean V_S model and associated model uncertainties at all grid points. Slices through the V_S model at various depths are plotted in Figure 10, and the corresponding V_S uncertainties at these depths are presented in Figure 11. Figure 12 presents six vertical cross sections through prominent crustal velocity anomalies in the western United States.

[31] Because a reference model is needed to identify velocity anomalies and no appropriate reference model exists for the region, we construct a regional V_S reference model for the western United States. Previous studies have made use of global 1-D reference models, such as ak135 [*Kennett et al.*, 1995], but the lower crustal and uppermost mantle velocities observed in the western United States are, on average, uniformly slow relative to these models. A western United States reference V_S model is constructed from the mean of the V_S models from all continental grid points in the study. It is plotted in Figure 13 and summarized in Table 3.

[32] The variation of the model laterally is compared to the spatially averaged uncertainty in V_S as a function of depth in Figure 14. Uncertainties are highest in the shallowest parts of the model, decrease through the upper and middle crust, and increase to values above 3% near the Moho between about 35 and 45 km depth. At these depths, lower crustal V_S trade-offs with crustal thickness (as described in section 2.2.4) and with V_S values in the uppermost mantle, contribute to increased model uncertainties. In the mantle, V_S uncertainties decrease to values between 1% and 1.5% between 60 and 175 km. On average, the root mean square (RMS) of model anomalies is more than twice the average model uncertainty except in the uppermost mantle between about 40 and 55 km and below 110 km depth. The decreased ratio of RMS anomalies to mean uncertainties generally

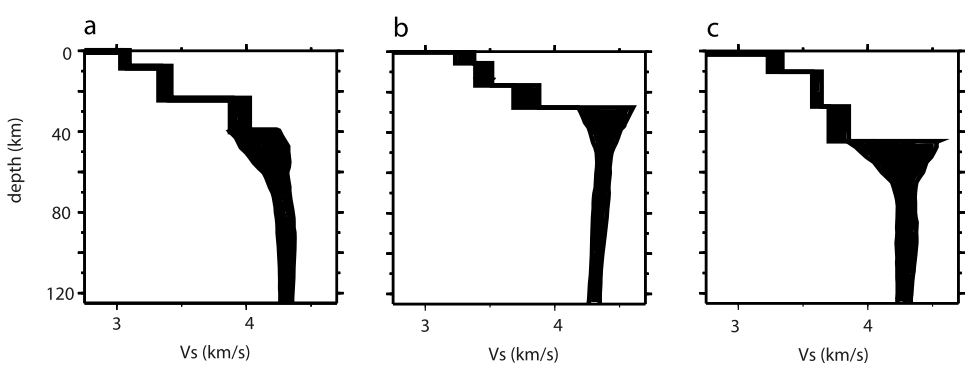

Figure 9. Examples of the isotropic V_S components of the radially anisotropic model m_1 for three different tectonic provinces. V_S models are presented for (a) the southern Cascadia back arc (239.0,42.5), (b) the Yakima Fold Belt (241.0,47.0), and (c) the Colorado Plateau (248.0,38.0), identified by blue squares in Figure 1.

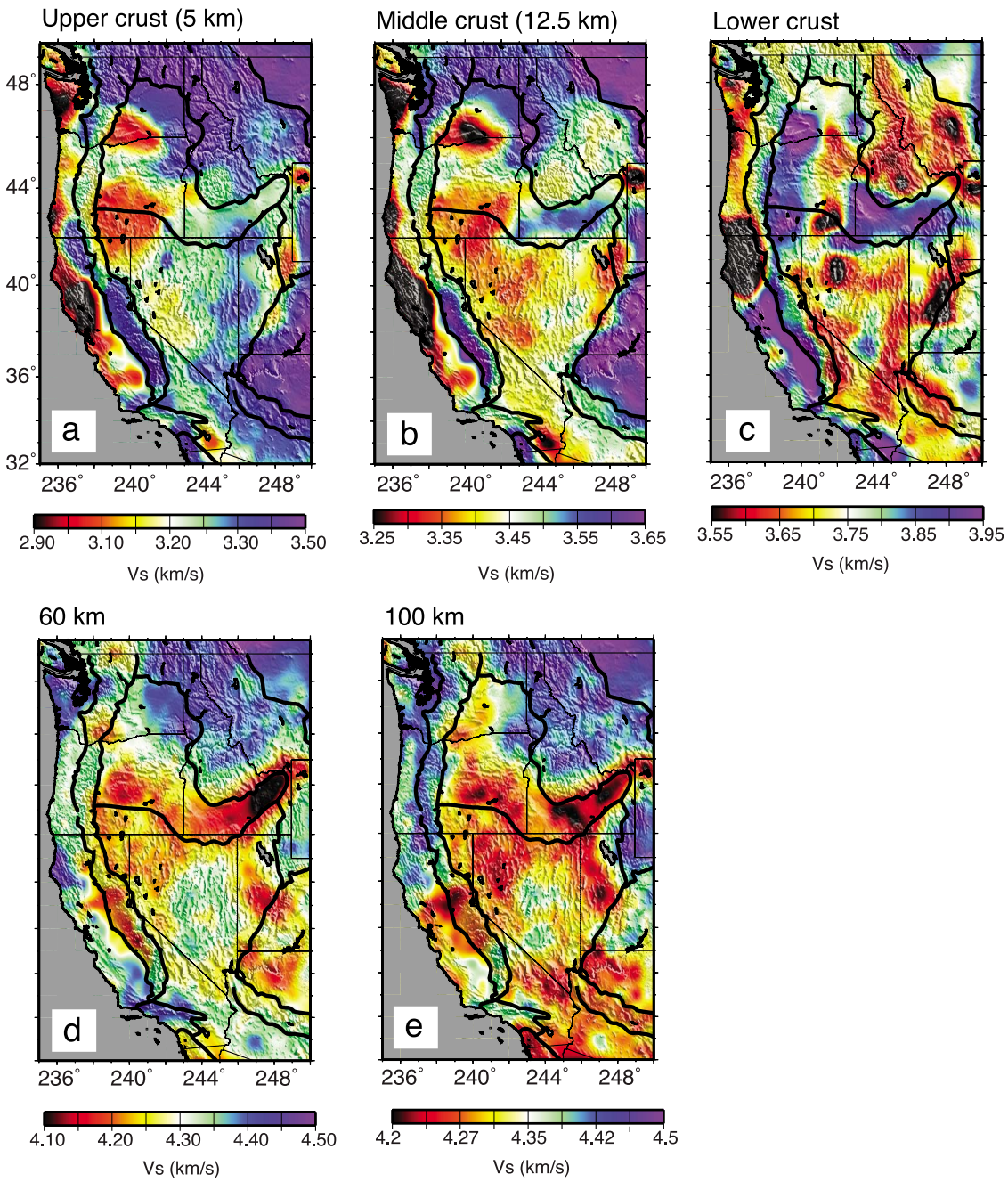

Figure 10. Depth slices through the western United States in which V_S has been computed from the radially anisotropic model by Voigt averaging. The mean shear wave velocities from the ensemble of accepted models are presented. Shear wave velocities are plotted for the (a) upper crust (5 km), (b) middle crust (12.5 km), (c) lower crust (variable depth, just above Moho), (d) 60 km depth, and (e) 100 km depth.

degrades our confidence in model anomalies from the Moho to about 50 km depth and at depths greater than 125 km. *Moschetti et al.* [2010] show that the mean amplitudes ($2|V_{SH} - V_{SV}|/(V_{SH} + V_{SV})$) of crustal and mantle radial anisotropy beneath the Basin and Range and Northern Rocky Mountains are about 3.5 and 5.5%, respectively. Because mean RMS velocity anomalies in the western United States are less than about 6%, except near the surface, neglecting the effects of crustal and upper mantle radial anisotropy may strongly bias the estimates of isotropic V_S significantly.

[33] To identify robust features in the V_S model, we interrogate the set of accepted models at each point for persistent model features. In previous discussions of anomaly persistence by *Shapiro and Ritzwoller* [2002] and *Yang et al.* [2008b], persistent model features are defined as those anomalies that exist in all accepted models. We modify this approach by identifying persistent anomalies relative to a reference model by a statistical hypothesis test. We pose as the null hypothesis that the absolute velocity difference between the V_S model for a given grid point and the western United States V_S reference model is less than the

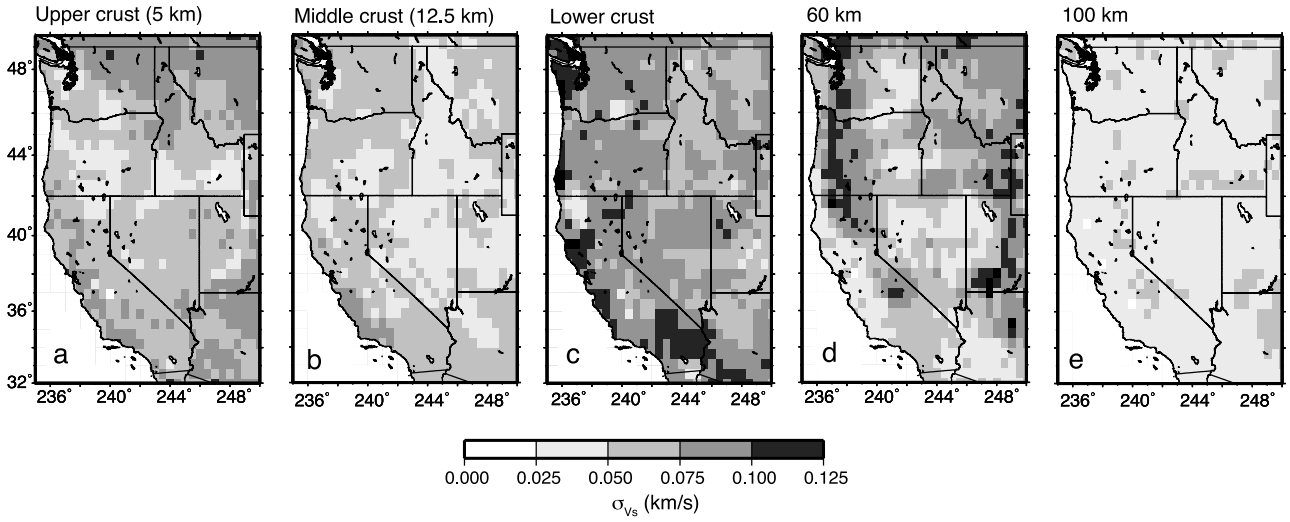

Figure 11. Uncertainty values associated with the shear wave velocity estimates of Figure 10 are plotted in absolute units for the (a) upper crust (5 km), (b) middle crust (12.5 km), (c) lower crust (variable depth, just above Moho), (d) 60 km depth, and (e) 100 km depth. Uncertainties are defined as the standard deviation of the ensemble of accepted models at each depth.

V_S uncertainty. Because the means, variances and populations of the western United States reference V_S model and the V_S models at all grid points are known, hypothesis testing is readily carried out with a Z test. Details of the test may be found elsewhere [e.g., *Freund*, 1999]. At grid points where the null hypothesis is rejected at the 95% confidence level, model anomalies are termed "persistent." Persistent features in the V_S model are contoured in Figure 12 with black lines.

[34] We identify here the primary, persistent features in the V_S depth slices. This identification is followed by a brief discussion of the prominent model features in section 4 below. In the upper crust (Figure 10a), high wave speeds are observed in the Sierra Nevada, Peninsular Range, Colorado Plateau, northern Cascade Range, and Columbia Plateau. Persistent low wave speeds are observed beneath the Olympic Peninsula, California Coast Range, western Nevada, Wasatch Range, through much of the southern Cascadia back-arc region, and beneath the Yakima Fold Belt.

[35] Middle crustal anomalies are presented in Figure 10b. High wave speeds exist in the Sierra Nevada, Peninsular, and northern Cascade Ranges, throughout the Colorado Plateau, and through much of the Columbia Plateau. At middle crustal depths, high wave speeds emerge throughout the Snake River Plain. Much of central and western Nevada show low wave speeds at middle crustal depths. The low wave speeds beneath the California Coast Ranges, western Nevada, and the Wasatch Range cover a greater area at this depth.

[36] In the lower crust, plotted in Figure 10c, the most prominent wave speed changes from the overlying crust are the emergence of high-velocity features underlying the Peninsular Range, the Great Central Valley of California, and the region immediately east of the Cascade Range. The Snake River Plain high-velocity anomaly becomes more pronounced, and the broad, middle crustal low-velocity anomaly covering much of Nevada and the Cascadia back-arc region contracts to distinct bands of low wave speed which run along the northern, eastern, and western boundaries of the Basin and Range. Low wave speeds underlie much of the Northern Rocky Mountain region.

[37] The uppermost mantle V_S structure (plotted at 60 and 100 km depths in Figures 10d and 10e) is characterized by four primary features; three high-velocity features and one large-scale low-velocity feature. High velocity anomalies include the subducting Juan de Fuca and Gorda slabs, the Proterozoic lithosphere underlying much of eastern Washington, northern Idaho and western Montana, and a high-velocity mantle anomaly associated with the southern Sierra Nevada Range and the Transverse Range. Low uppermost mantle wave speeds underlie the region encompassing the Cascadia back arc, the Sierra Nevada, much of Nevada, the Wasatch Range and the Snake River Plain. Uppermost mantle shear wave velocities beneath the Snake River Plain and the Cascadia back arc are particularly slow.

3.3. Data Misfit From the V_S models

[38] The χ^2 misfit of isotropic model m_0 is plotted in Figure 15a. Mean χ^2 misfit is 8.7 across the map. The Basin and Range and the Northern Rocky Mountains show particularly poor data fits. Misfit from this model is analyzed in depth by *Moschetti et al.* [2010], which shows that misfit across the western United States results from a crustal Rayleigh-Love discrepancy. At these points, the dispersion curves predicted from the isotropic V_S model at periods that are most sensitive to the crust are too fast for the Rayleigh wave observations and too slow for the Love wave observations.

[39] *Moschetti et al.* [2010] also demonstrate that the simultaneous inversion of short-period (<30 s) Rayleigh and Love wave dispersion data from much of the western United States requires the introduction of radial anisotropy in the crust and upper mantle to reduce the χ^2 misfit observed from the isotropic V_S model and to resolve the Rayleigh-Love discrepancy. For model m_1, which results from the

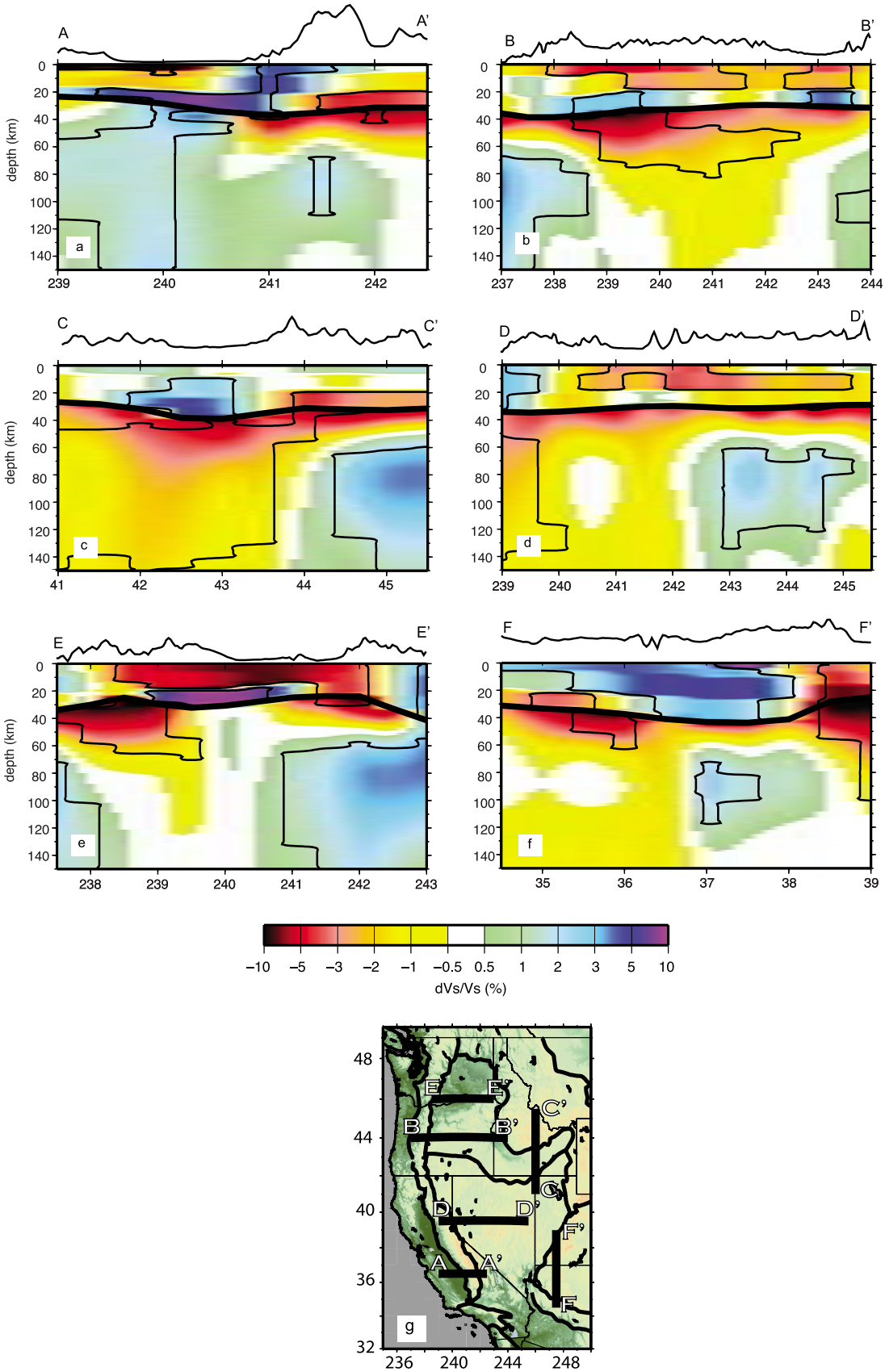

Figure 12

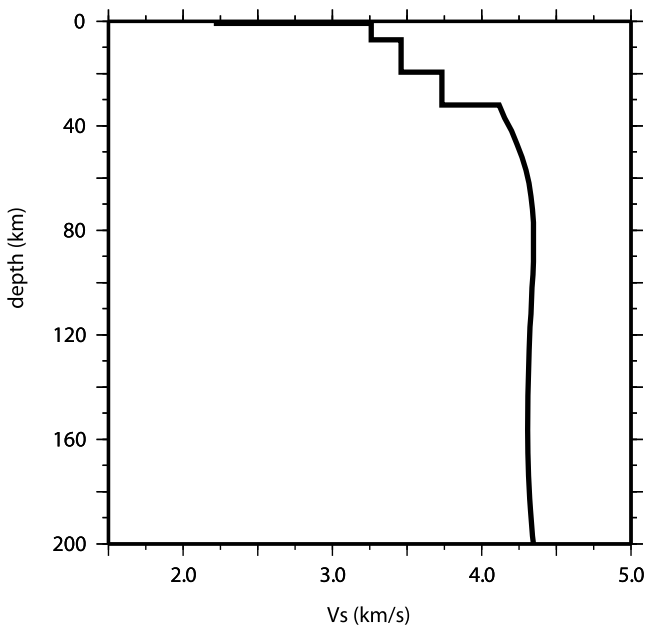

Figure 13. Western United States average (reference) V_S model. The reference V_S model is constructed from the mean of all continental models in the western United States. Crustal parameters are given in Table 2.

radially anisotropic V_S inversion, mean χ^2 misfit across the region is reduced to 2.4 from 8.7. The χ^2 values of the best fitting radially anisotropic V_S models are plotted in Figure 15b. The dispersion data across 90% of the study region is fit at a χ^2 value of 4 or better by the radially anisotropic V_S model.

[40] Several regions, however, remain poorly fit by a radially anisotropic V_S model with the given model parameterization and a priori constraints. These regions include the Olympic Peninsula, Mendocino Triple Junction, southern Cascadia back arc, Yakima Fold Belt, Salton Trough, Snake River Plain, California Great Central Valley, Wasatch Range, and Yellowstone. Because the longer-period (>30 s) Rayleigh wave measurements are generally well fit by the radially anisotropic V_S model, we present a plot of χ^2 misfit in the 6–30 s period band in Figure 15c to highlight the regions where the dispersion measurements with the strongest sensitivities to crustal V_S structure are poorly fit. We refer to the 6–30 s period band χ^2 misfit map, Figure 15c, as a plot of "crustal misfit."

[41] Characteristic dispersion curve misfits from the radially anisotropic V_S model m_1 to the dispersion data for the poorly fit regions are presented in Figure 16. Because Yellowstone is located at the edge of the inversion region, where the resolution of the dispersion maps degrades, we postpone discussion of this feature until data coverage and resolution in this region improves. Rayleigh wave phase speeds are generally well fit even in these regions. However, the observed Rayleigh wave phase speeds are slower than model-predicted phase speeds in the Yakima Fold Belt (Figure 16d) and Great Central Valley (Figure 16e). The Rayleigh wave group speeds below about 15 s period are generally slow relative to the model-predicted values except in the Mendocino Triple Junction (Figure 16a), Olympic Peninsula (Figure 16b), and southern Cascadia back-arc (Figure 16c) regions where the Rayleigh wave group speeds contain local maxima below 20 s period that are not well fit by the final V_S model. The Love wave phase speeds below 15 s period are notably fast, relative to the data for the Olympic Peninsula (Figure 16b), southern Cascadia back arc (Figure 16c) and Snake River Plain (Figure 16g). Model-predicted Love wave phase speeds are slow at these periods in the Great Central Valley (Figure 16e) and Wasatch Range (Figure 16h). Although the V_S model allows for radial anisotropy in the middle and lower crust, we note that a Rayleigh-Love discrepancy remains in the data misfits from the Yakima Fold Belt and the Wasatch Range (Figures 16d and 16h).

[42] We identify two general classes of data misfit in the characteristic data misfit plots in Figure 16.

[43] 1. The first class of structure is at grid points where data misfit is greatest at short periods (<15 s) and increases with decreasing period. Because misfit occurs primarily at the shortest periods, where the dispersion curves are most sensitive to the shallowest velocity structures, the model parameterization in the upper and middle crust needs to be modified. Data misfits from the Yakima Fold Belt, Great Central Valley, Snake River Plain, and Wasatch Range belong to this class.

[44] 2. The second class of structure is at grid points where data misfits are greatest at intermediate periods (15–30 s), including the data misfits from the Mendocino Triple Junction, Olympic Peninsula, southern Cascadia back-arc, and Salton Trough regions. In these cases, the models underpredict the Rayleigh wave group speeds between about 10 and 15 s period. For the first three regions listed, this misfit characteristic in the Rayleigh wave group speeds coincides with minima in the group speed curves at longer periods (>25 s). This intermediate period Airy phase may indicate a small to negative gradient in the V_S depth profile and suggests that crustal low-velocity zone parameterizations may be needed. In the Salton Trough region, the shortest (<10 s) and longer (>25 s) periods are well fit, but the intermediate periods are slow for all wave types. Alternative midcrustal model parameterizations may be more appropriate for this region.

4. Discussion of the Isotropic 3-D V_S Model

[45] Although the models m_0 and m_1 include mantle V_S structure, we focus discussion on persistent V_S anomalies in

Figure 12. Vertical cross sections through the western United States V_S model. Velocities are plotted relative to the western United States reference model presented in Figure 13. Surface and Moho topography are plotted on each cross section as black lines above and superimposed over the velocity anomaly plots, respectively. West-east cross sections are plotted for latitudes (a) 36.5°, (b) 44.0°, (d) 39.5°, and (e) 46.0°. South-north cross sections are plotted along longitudes (c) 246° and (f) 247.5°. Persistent features are outlined with black contours. (g) The locations of the cross-sections in Figures 12a–12f are plotted and labeled.

Table 3. Western United States Reference V_S Crustal Model

Model Parameter	Value
Sediment thickness	750 m
Crustal thickness	32.0 km
V_S sediments	1.95 km/s
V_S layer 1	3.27 km/s
V_S layer 2	3.47 km/s
V_S layer 3	3.74 km/s
V_P/V_S sediment layer	2.10 km/s
V_P/V_S crystalline crust	1.78 km/s

the crust because mantle features have already been discussed by *Yang et al.* [2008b]. The interpretation of all persistent model features is beyond the scope of the paper. In particular, the V_S structure of Cascadia is examined, separately, in the work of M. P. Moschetti and M. H. Ritzwoller (Lower crustal fluids in the Cascadia forearc: Insight from surface wave tomography, manuscript in preparation, 2010). We identify the following principal, persistent crustal features for discussion here: (1) the California Coast Ranges, Great Central Valley, and Sierra Nevada Range; (2) the lower crustal velocity anomalies beneath the Cascadia back arc, Snake River Plain and the High Lava Plains; (3) the crustal structure of the Basin and Range province in Nevada; (4) the enigmatic Yakima Fold Belt; and (5) the Colorado Plateau.

4.1. California Coast Ranges, Great Central Valley, and Sierra Nevada Range

[46] Terrane accretion at the edge of the western Cordillera and emplacement of the Sierra Nevada batholith during Mesozoic arc volcanism led to the development of the present-day California Coast Ranges-Great Central Valley-Sierra Nevada structures [*Saleeby and Busby-Spera*, 1992]. In our model, the Coast Ranges throughout California are slow through the upper and middle crust, and the lower crust of the Coast Range is distinguished from the lower crust beneath the Great Central Valley by its relatively slower wave speeds. This observation is consistent with the interpretation of later-stage mélange accretion [*Dickinson*, 2008]. Beneath the Great Central Valley, low wave speeds are associated with the thick sediment packages of the San Joaquin Basin in the south and Sacramento Basin in the north (Figures 10a and 12a). The Great Central Valley is underlain by a high-velocity lower crust, which is offset to the west from the Sierra Nevada Range. This feature underlies the entire Great Central Valley and has been interpreted as oceanic lithosphere, which may be underlain by continental crust [*Godfrey et al.*, 1997]. The Sierra Nevada Range is bounded to the east by the neutral to low wave speeds in the crust beneath the western margin of the Basin and Range (Walker Lane). There is little variation in shear wave velocity with depth within the Sierra Nevada.

4.2. Lower Crustal Wave Speeds of the Cascadia Back Arc, Snake River Plain, and High Lava Plains

[47] The high wave speed anomalies east of the Cascade volcanic arc and beneath the Snake River Plain (see Figures 12b and 12c) are the most prominent lower crustal velocity features in the northern section of the model. The entire region is underlain by a broad low wave speed anomaly in the uppermost mantle encompassing the Cascadia back arc and Yellowstone hot spot track [*Smith and Braile*, 1994]. The slow wave speeds in the uppermost mantle are strongly correlated with locally high heat flow [*Blackwell and Richards*, 2004], and we infer that the uppermost mantle in this region is relatively warm. Within the Snake River Plain, *Peng and Humphreys* [1998] and *Stachnik et al.* [2008] find evidence for a midcrustal sill and a low-velocity zone in the lower crust beneath the Snake River Plain caused by the northeastward progression of the Yellowstone hot spot between about 12.5–10 Ma [*Pierce and Morgan*, 1989]. Our model is consistent with the interpretation of emplacement of high-velocity material in the middle to lower crust that is perhaps chemically distinct from surrounding crust. Although data misfit from our model is not improved by allowing a crustal low-velocity zone with the current crustal parameterization, the relatively high crustal misfits through the Snake River Plain and southern Cascadia back-arc region suggest that a modification in the crustal velocity parameterization in this region is warranted.

[48] Previous seismic studies have variously interpreted the high wave speed lower crustal anomaly, which runs along the entire eastern edge of the Cascade Range in our model, as a Mesozoic subduction zone backstop and magmatic arc [*Fuis*, 1998; *Fuis et al.*, 1987], crustal underplating [*Catchings and Mooney*, 1988a] and as a lower crustal intrusion and modification caused by continental rifting [*Catchings and Mooney*, 1988b]. We propose that the high-

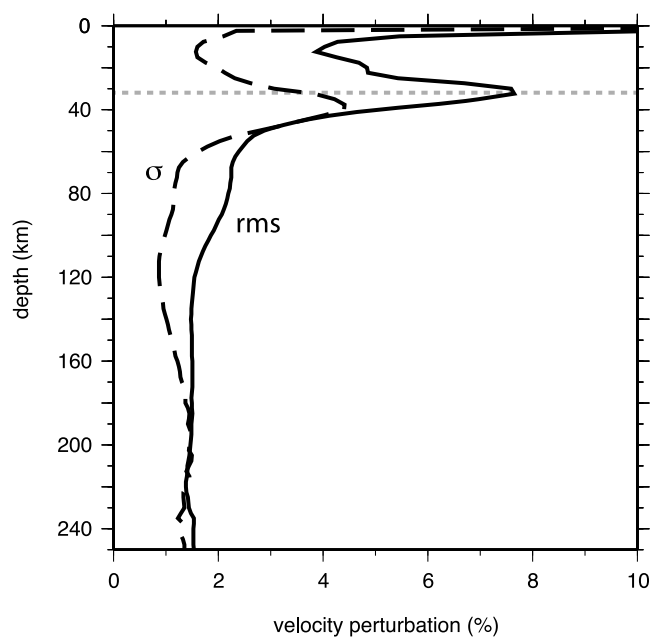

Figure 14. RMS lateral variation of the model and spatially average mean model uncertainty are plotted versus depth. Uncertainties are lowest in the middle crust and in the mantle at depths between about 60 and 150 km. RMS model anomalies are about twice the mean model uncertainty value, except between 30 and 55 km depth and below 110 km. Velocity trade-offs between the lower crust and mantle contribute to mean uncertainties greater than 2.5% from 30 to 45 km depth. The regionally averaged Moho depth is plotted with a dashed gray line.

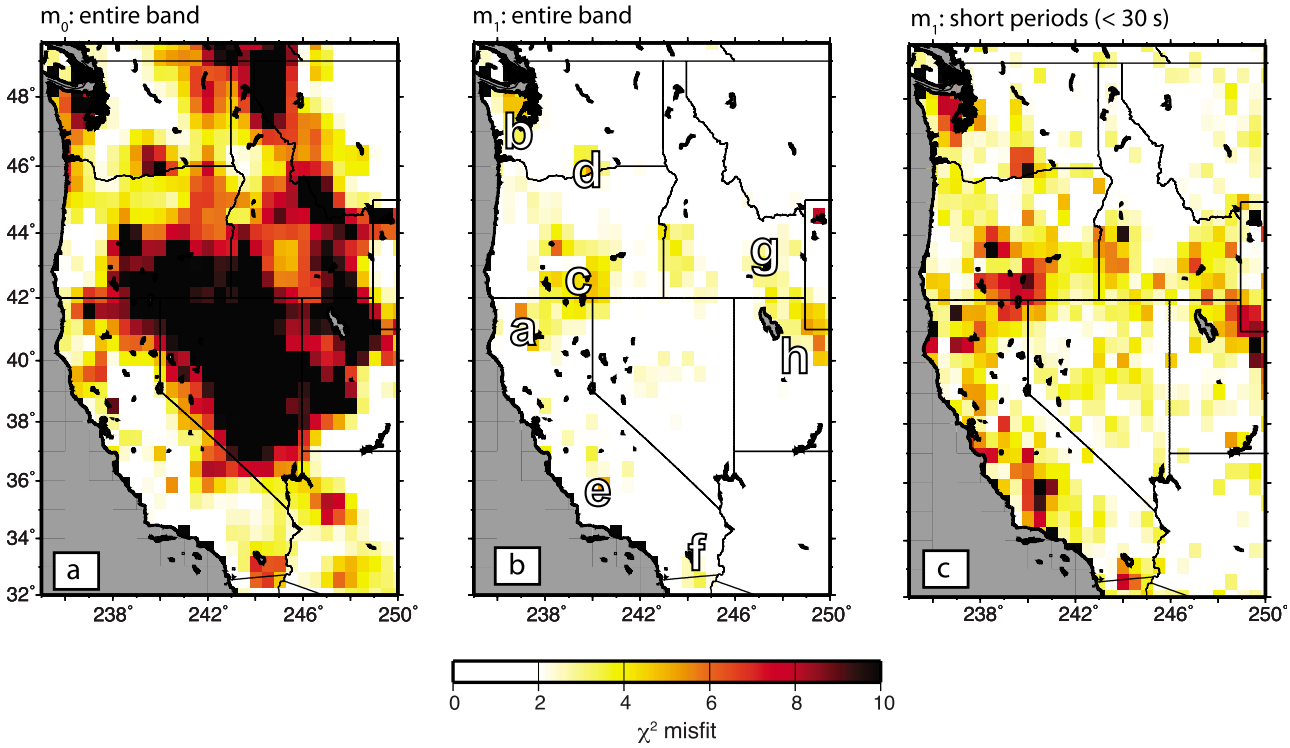

Figure 15. The χ^2 values corresponding to the best fitting isotropic (m_0) and radially anisotropic (m_1) V_S models across the entire period band and within the 6–30 s period band for the radially anisotropic V_S model. (a) Entire band χ^2 values from the isotropic V_S model, m_0, show poor fit across large regions of the western United States, particularly in extensional provinces such as the Basin and Range. The mean χ^2 value across the study region is 8.7. (b) Introduction of radial anisotropy to the crust and upper mantle in model m_1 reduces the regionally averaged entire band χ^2 value to 2.4. (c) Short-period χ^2 values in the 6–30 s period band for the radially anisotropic V_S model m_1. Short-period dispersion measurements have strong sensitivity to the crust; thus, we refer to this plot as the "crustal misfit". Regions of poor short-period fit include the Olympic Peninsula, Mendocino Triple Junction, southern Cascadia back arc, Yakima Fold Belt, Salton Trough, Snake River Plain, California Great Central Valley, Wasatch Range, and Yellowstone. The letter labels in Figure 15b are also used in Figure 16.

velocity lower crustal features east of the Cascade Range and within the Snake River Plain result from mafic crustal intrusions or crustal underplating caused by partial melting of warm uppermost mantle. Across this region, the lower crust beneath eastern Oregon is distinguished by its reduced wave speed relative to neighboring high-velocity anomalies.

[49] The High Lava Plains of southeastern Oregon have experienced recent volcanism along a northwest younging track, which mirrors the Yellowstone hot spot-related calderas of the Snake River Plain [*Jordan et al.*, 2004]. The relatively depressed wave speeds of the lower crust in this region may result from compositional and/or thermal modifications to the crust caused by magma injection or conductive heating. The region has been extensively studied in recent years [e.g., *Xue and Allen*, 2006; *Roth et al.*, 2008; *Warren et al.*, 2008]. Figure 12b presents a cross section through the region, along 44° latitude from the Cascade Range to the western Snake River Plain, which shows the neutral lower crustal wave speeds beneath eastern Oregon that increase to the west and east.

4.3. Crustal Structure of the Basin and Range in Northern Nevada

[50] Nevada has experienced a complex geologic history, including significant crustal deformation. The Basin and Range province is currently extending at about 1 cm/yr [*Thatcher et al.*, 1999] and has extended on average by about a factor of two during the late Cenozoic Era [*Wernicke*, 1992]. However, the isotropic V_S model shows relatively uniform crustal and mantle structure across northern Nevada at 39.5° latitude (see Figure 12d). Mean middle and lower crustal V_S values are about 3.4 and 3.6 km/s, respectively. Previous studies have identified the presence of a strongly reflecting lower crustal body throughout much of Nevada and a thin, very high wave speed anomaly at the base of the crust [*Potter et al.*, 1987; *McCarthy and Thompson*, 1988; *Benz et al.*, 1990]. We find no evidence in the isotropic V_S values of the model for large velocity discontinuities in the crust. However, as discussed by *Moschetti et al.* [2010], the correlation between the regions with high amplitudes of crustal radial anisotropy and significant Cenozoic extension, which is consistent with the alignment of anisotropic crustal minerals, may be a cause for

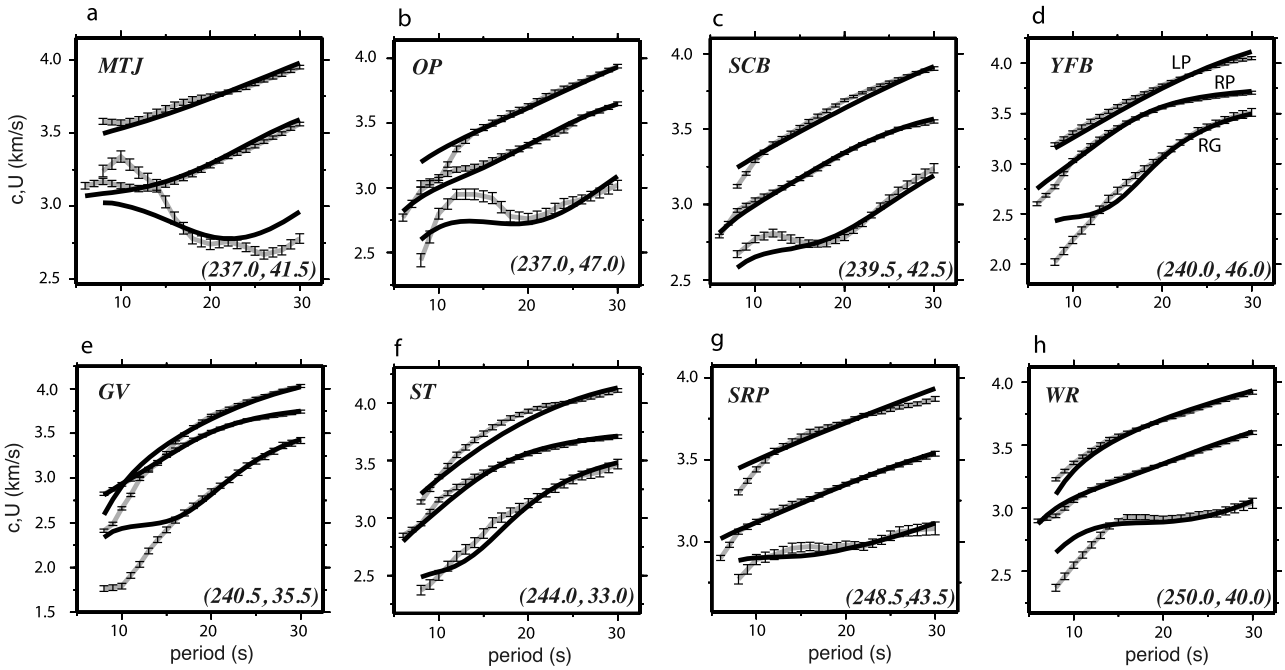

Figure 16. Characteristic short-period surface wave dispersion curve misfits from the radially anisotropic V_S model. The best fitting dispersion curves are plotted in black. Local dispersion curves and uncertainties are plotted with error bars and gray curves. The RP, RG, and LP labels in Figure 16d refer to the Rayleigh wave phase and group speeds and Love wave phase speeds, respectively. Grid point inversion examples from the following regions in the western United States are presented: (a) Mendocino Triple Junction (MTJ), (b) Olympic Peninsula (OP), (c) southern Cascadia back arc (SCB), (d) Yakima Fold Belt (YFB), (e) Great Central Valley (GV), (f) Salton Trough (ST), (g) Snake River Plain (SRP), and (h) Wasatch Range (WR). The locations corresponding to the plotted dispersion curves are identified by the letters plotted in Figure 15b.

the reflective lower crust [*McCarthy and Thompson*, 1988]. No evidence for a thin high-velocity layer at the base of the crust exists in our model. We acknowledge, however, that the crust contains finer-scale structures than can be resolved with surface waves because of the poor sensitivity that surface waves have to the large seismic impedance contrasts that are expected for a thin, high-velocity layer.

4.4. Yakima Fold Belt

[51] The distinctive crustal velocity structure of the Yakima Fold Belt arises from the effects of volcanic flows and deformation of a deep sedimentary basin [*Campbell and Bentley*, 1981]. Figure 12e presents a cross section from the Cascade Range, through the Yakima Fold Belt, to the Columbia Plateau in eastern Washington. Within the Yakima Fold Belt, our model shows very low wave speeds in the middle crust and low wave speeds in the upper crust. This structure has been interpreted to result from the capping of a deep sedimentary basin by basalt flows of the Columbia River Basalt Group between about 17–14.5 Ma [*Catchings and Mooney*, 1988b, *Tolan et al.*, 1989]. The decreased wave speeds of the lower crust, which overlie the Proterozoic mantle lithosphere beneath eastern Washington, suggest that lower crustal modification in this region was impeded by the rheologically strong lithospheric root. *Catchings and Mooney* [1988b] imaged the sediments of the Pasco Basin, which underlie 3–6 km of basalt, and a high-velocity lower crustal body. They proposed that the structure results from continental rifting. Our model is generally consistent with their observations, but our observation of the high-velocity lower crustal feature east of the Cascade Range extending from the southern Cascadia back arc to the Yakima Fold Belt suggests that the high wave speed anomaly in the lower crust beneath the Yakima Fold Belt may be caused by widespread crustal intrusions and under-plating related to the dynamics of the Cascadia subduction zone.

4.5. Colorado Plateau

[52] Figure 12f presents a cross-section along 247.5° longitude that traverses the western Colorado Plateau from south to north. The crust throughout the Colorado Plateau shows little variation in V_S with depth. At upper and middle crustal depths, V_S is fast and has been inferred to result from the mafic composition of the plateau [*Zandt et al.*, 1995]. North of the plateau, the crustal wave speeds of the Wasatch Range are uniformly low. The low wave speeds of the uppermost mantle that flank the Colorado Plateau are consistent with observations of late Cenozoic basaltic eruptions [*Best and Brimhall*, 1974]. At the southern end of the cross-section, the transition zone between the southern Basin and Range province and the Colorado Plateau shows neutral to low wave speeds in the middle to lower crust. It remains unclear whether the lower crustal wave speeds adjacent to

the Colorado Plateau result from thermal or compositional effects.

4.6. Anomalous Misfit Regions

[53] Although 90% of the study region is fit by a simple V_S model of the crust and uppermost mantle, high data misfits remain at 10% of the model grid points. The grid points with significant misfit at the short periods consistent with a crustal origin can be organized into eight geologic regions: (1) the Olympic Peninsula, (2) Mendocino Triple Junction, (3) southern Cascadia back arc and High Lava Plains, (4) Yakima Fold Belt, (5) Salton Trough, (6) Snake River Plain, (7) California Great Central Valley, and (8) Wasatch Range. Because these regions are geologically complex and the current model parameterization is not able to fit the observed data well, further investigation into the V_S structure of these regions is required.

[54] We suggest three modifications to the current model parameterization to improve the data misfit from these regions: (1) breaking the constraint that crustal shear wave velocities increase monotonically with depth, (2) introducing thinner crustal layers, and (3) including the effect of radial anisotropy in the upper crust. Except in California's Great Central Valley, where sediment thicknesses are significantly greater than average, sensitivity tests suggest that perturbations to the V_S structure of the sediment layer are unlikely to resolve the observed data misfits. The first data misfit class, defined in section 3.3, is likely to show improved fit to the data by modifying the parameterization of the upper to middle crustal layers. In contrast, the second data misfit class is likely to be improved by varying model parameterization at the depths of the middle and lower crustal layers. Moschetti and Ritzwoller (manuscript in preparation, 2010) examine the effect on χ^2 misfit of breaking the monotonic crustal velocity constraint within the Cascadia fore-arc, arc and back-arc regions and find that the misfit to the dispersion data from the Cascadia fore arc beneath northern California is improved by the introduction of a crustal low-velocity zone.

5. Conclusions

[55] A radially anisotropic inversion of Rayleigh and Love wave dispersion measurements from Ambient Noise Tomography (ANT) and Multiple Plane Wave Tomography (MPWT) is carried out to construct an isotropic 3-D V_S model of the crust and uppermost mantle beneath the western United States. Because the data are inverted by a Monte Carlo method, model uncertainties accompany the model and allow for the identification of persistent model features by statistical hypothesis testing. Model uncertainties peak below the Moho and reduce confidence in the uppermost mantle V_S estimates from the base of the crust to about 55 km depth, but persistent isotropic anomalies exist at all crustal depths across the western United States.

[56] Although the velocity structure of the upper mantle beneath the western United States consists of only four principal large-scale shear wave velocity features, the overlying continental crust contains far greater heterogeneity. We infer that the high wave speed anomalies of the lower crust result primarily from mafic compositions caused by intrusion, under-plating or accretion. The low wave speed anomalies of the lower crust beneath the Basin and Range, High Lava Plains and eastern California are inferred to be thermally depressed wave speed features caused by conductive heating. At middle crustal depths, accretionary prisms and mélange show the lowest wave speeds. Middle crustal high wave speed anomalies are caused by both compositional effects, for example, the basalts of the Columbia River flood basalt group and throughout the Snake River Plain, and crystalline effects, as seen in the granitoids of the Sierra Nevada. In general, the upper and middle crustal wave speed anomalies are correlated. Prominent exceptions to this correlation include the Snake River Plain, Northern Rocky Mountains and eastern Basin and Range. The velocity structure of the middle and lower crust beneath the Snake River Plain is consistent with a mafic intrusion caused by the passing Yellowstone hot spot. The cause of the wave speed differences in the upper and middle to lower crust beneath the Northern Rocky Mountains and the Basin and Range (Figures 10a–10c) remains enigmatic. The amplitudes of the observed velocity anomalies are similar to the amplitudes of radial anisotropy for the crust and uppermost mantle found by *Moschetti et al.* [2010], so that radial anisotropy cannot be ignored in the construction of an isotropic V_S model either in the crust or upper mantle.

[57] The vast majority (90%) of the western United States is well fit by a radially anisotropic V_S model with the parameterization discussed in section 2.2.1 where crustal velocities increase monotonically with depth. However, this simple model parameterization is not sufficient to fit all dispersion curves in the western United States, and high crustal misfit is observed in the Olympic Peninsula, Mendocino Triple Junction, southern Cascadia back arc, Yakima Fold Belt, Salton Trough, Snake River Plain, California Great Central Valley, and Wasatch Range. Future work is needed to investigate the effect of different crustal parameterizations on data misfit in these regions. The inversion method presented here naturally lends itself to the incorporation of longer-period (>32 s) Love wave measurements for improved constraints on mantle radial anisotropy and to the inversion of emerging data from the TA to extend the model to a continental scale crustal V_S model.

[58] **Acknowledgments.** The authors thank two anonymous reviewers and the editors for their insightful comments. Malcolm Sambridge provided the Neighborhood Algorithm code. Research support from the National Science Foundation (NSF) (EAR-0450082 and EAR-0711526) and an NDSEG Fellowship from the American Society for Engineering Education to M.P.M. are acknowledged. The facilities of the IRIS Data Management System and specifically the IRIS Data Management Center were used to access the waveform and metadata required in this study. The IRIS DMS is funded by the NSF and specifically the GEO Directorate through the Instrumentation and Facilities Program of the NSF under Cooperative Agreement EAR-0552316.

References

Babuska, V., and M. Cara (1991), *Seismic Anisotropy in the Earth*, Kluwer Acad., Dordrecht.

Barmin, M. P., M. H. Ritzwoller, and A. L. Levshin (2001), A fast and reliable method for surface wave tomography, *Pure Appl. Geophys.*, *158*(8), 1351–1375, doi:10.1007/PL00001225.

Bensen, G. D., M. H. Ritzwoller, M. P. Barmin, A. L. Levshin, F. Lin, M. P. Moschetti, N. M. Shapiro, and Y. Yang (2007), Processing seismic ambient noise data to obtain reliable broad-band surface wave dispersion measurements, *Geophys. J. Int.*, *169*, 1239–1260, doi:10.1111/j.1365-246X.2007.03374.x.

Bensen, G. D., M. H. Ritzwoller, and N. M. Shapiro (2008), Broad-band ambient noise surface wave tomography across the United States, *J. Geophys. Res.*, *113*, B05306, doi:10.1029/2007JB005248.

Bensen, G. D., M. H. Ritzwoller, and Y. Yang (2009), A 3D shear velocity model of the crust and uppermost mantle beneath the United States from ambient seismic noise, *Geophys. J. Int.*, *117*(3), 1–12.

Benz, H. M., R. B. Smith, and W. D. Mooney (1990), Crustal structure of the northwestern Basin and Range province from the 1986 program for array seismic studies of the continental lithosphere seismic experiment, *J. Geophys. Res.*, *95*(B13), 21,823–21,842, doi:10.1029/JB095iB13p21823.

Best, M. G., and W. H. Brimhall (1974), Late Cenozoic alkalic basaltic magmas in the western Colorado Plateaus and the Basin and Range Transition Zone, U.S.A., and their bearing on mantle dynamics, *Geol. Soc. Am. Bull.*, *85*(11), 1677–1690, doi:10.1130/0016-7606(1974)85<1677:LCABMI>2.0.CO;2.

Blackwell, D. D., and M. Richards (2004), Geothermal map of North America, 1 sheet, scale 1:6,500,000, Am. Assoc. of Pet. Geol., Tulsa, Okla.

Brenguier, F., N. M. Shapiro, M. Campillo, A. Nercessian, and V. Ferrazzini (2007), 3-D surface wave tomography of the Piton de la Fournaise volcano using seismic noise correlations, *Geophys. Res. Lett.*, *34*, L02305, doi:10.1029/2006GL028586.

Brocher, T. (2005), Empirical relations between elastic wavespeeds and density in the Earth's crust, *Bull. Seismol. Soc. Am.*, *95*(6), 2081–2092, doi:10.1785/0120050077.

Burdick, S., C. Li, V. Martynov, T. Cox, J. Eakins, L. Astiz, F. Vernon, G. Pavlis, and R. van der Hilst (2008), Upper mantle heterogeneity beneath North America from travel time tomography with global and USArray Transportable Array data, *Seismol. Res. Lett.*, *79*(3), 384–392, doi:10.1785/gssrl.79.3.384.

Campbell, N. P., and R. D. Bentley (1981), Late Quaternary deformation of the Toppenish Ridge uplift in south-central Washington, *Geology*, *9*, 519–524, doi:10.1130/0091-7613(1981)9<519:LQDOTT>2.0.CO;2.

Catchings, R. D., and W. D. Mooney (1988a), Crustal structure of east central Oregon: Relation between Newberry Volcano and regional crustal structure, *J. Geophys. Res.*, *93*(B9), 10,081–10,094, doi:10.1029/JB093iB09p10081.

Catchings, R. D., and W. D. Mooney (1988b), Crustal structure of the Columbia Plateau: Evidence for Continental Rifting, *J. Geophys. Res.*, *93*(B1), 459–474, doi:10.1029/JB093iB01p00459.

Cho, K. H., R. B. Herrmann, C. J. Ammon, and K. Lee (2007), Imaging the upper crust of the Korean Peninsula by surface-wave tomography, *Bull. Seismol. Soc. Am.*, *97*(1B), 198–207, doi:10.1785/0120060096.

Christensen, N., and W. D. Mooney (1995), Seismic velocity structure and composition of the continental crust: A global view, *J. Geophys. Res.*, *100*(B6), 9761–9788, doi:10.1029/95JB00259.

Dickinson, W. R. (2008), Accretionary Mesozoic-Cenozoic expansion of the Cordilleran continental margin in California and adjacent Oregon, *Geosphere*, *4*(2), 329–353, doi:10.1130/GES00105.1.

Dziewonski, A. M., and D. L. Anderson (1981), Preliminary reference Earth model, *Phys. Earth Planet. Inter.*, *25*(4), 297–356, doi:10.1016/0031-9201(81)90046-7.

Forsyth, D. W., and A. Li (2005), Array-analysis of two-dimensional variations in surface wave phase velocity and azimuthal anisotropy in the presence of multipathing interference, in *Seismic Earth: Array Analysis of Broadband Seismograms*, vol. 157, edited by A. Levander and G. Nolet, pp. 81–97, AGU, Washington, D. C.

Freund, J. (1999), *Mathematical Statistics*, 6th ed., Prentice Hall, Upper Saddle River, N.J.

Fuis, G. (1998), West margin of North America—A synthesis of recent seismic transects, *Tectonophysics*, *288*(1–4), 265–269, doi:10.1016/S0040-1951(97)00300-4.

Fuis, G., T. Ryberg, N. Godfrey, D. Okaya, and J. Murphy (2001), Crustal structure and tectonics from the Los Angeles basin to the Mojave Desert, southern California, *Geology*, *29*(1), 15–18, doi:10.1130/0091-7613(2001)029<0015:CSATFT>2.0.CO;2.

Fuis, G. S., J. J. Zucca, W. D. Mooney, and B. Milkereit (1987), A geologic interpretation of seismic-refraction results in northeastern California, *Geol. Soc. Am. Bull.*, *98*(1), 53–65, doi:10.1130/0016-7606(1987)98<53:AGIOSR>2.0.CO;2.

Gilbert, H. J., and M. Fouch (2007), Complex upper mantle seismic structure across the southern Colorado Plateau/Basin and Range: II. Results from receiver function analysis, *Eos Trans. AGU*, *88*(52), Fall Meet. Suppl., Abstract S41B-0558.

Gilbert, H. J., and A. F. Sheehan (2004), Images of crustal variations in the intermountain west, *J. Geophys. Res.*, *109*, B03306, doi:10.1029/2003JB002730.

Godfrey, N. J., B. C. Beaudoin, S. L. Klemperer, and M. W. Group (1997), Ophiolitic basement to the Great Valley forearc basin, California, from seismic and gravity data: Implications for crustal growth at the North American continental margin, *Geol. Soc. Am. Bull.*, *109*(12), 1536–1562, doi:10.1130/0016-7606(1997)109<1536:OBTTGV>2.3.CO;2.

Grand, S. P. (1994), Mantle shear structure beneath the Americas and surrounding oceans, *J. Geophys. Res.*, *99*(B6), 11,591–11,621, doi:10.1029/94JB00042.

Herrmann, R. B., and C. J. Ammon (2004), *Computer Programs in Seismology: Surface Waves, Receiver Functions and Crustal Structure*, St. Louis Univ., St. Louis, Mo.

James, M. B., and M. H. Ritzwoller (1999), Feasibility of truncated perturbation expansions to approximate Rayleigh wave eigenfrequencies and eigenfunctions in heterogeneous media, *Bull. Seismol. Soc. Am.*, *89*, 433–442.

Jordan, B., A. Grunder, R. Duncan, and A. Deino (2004), Geochronology of age-progressive volcanism of the Oregon High Lava Plains: Implications for the plume interpretation of Yellowstone, *J. Geophys. Res.*, *109*, B10202, doi:10.1029/2003JB002776.

Kennett, B. L. N., E. R. Engdahl, and R. Buland (1995), Constraints on seismic velocities in the Earth from traveltimes, *Geophys. J. Int.*, *122*(1), 108–124, doi:10.1111/j.1365-246X.1995.tb03540.x.

Laske, G., and G. Masters (1997), A global digital map of sediment thickness, *Eos Trans. AGU*, *78*, 483.

Lin, F., M. H. Ritzwoller, J. Townend, M. Savage, and S. Bannister (2007), Ambient noise Rayleigh wave tomography of New Zealand, *Geophys. J. Int.*, *170*(2), 649–666, doi:10.1111/j.1365-246X.2007.03414.x.

Lin, F., M. P. Moschetti, and M. H. Ritzwoller (2008), Surface wave tomography of the western United States from ambient seismic noise: Rayleigh and Love wave phase velocity maps, *Geophys. J. Int.*, *173*(1), 281–298, doi:10.1111/j.1365-246X.2008.03720.x.

Lin, F., M. H. Ritzwoller, and R. Snieder (2009), Eikonal tomography: Surface wave tomography by phase-front tracking across a regional broad-band seismic array, *Geophys. J. Int.*, *177*(3), 1091–1110, doi:10.1111/j.1365-246X.2009.04105.x.

Lobkis, O. I., and R. L. Weaver (2001), On the emergence of the Green's function in the correlations of a diffuse field, *J. Acoust. Soc. Am.*, *110*(6), 3011–3017, doi:10.1121/1.1417528.

Love, A. (1927), *A Treatise on the Theory of Elasticity*, 4th ed., Cambridge Univ., Cambridge.

Marone, F., Y. Gung, and B. Romanowicz (2007), Three-dimensional radial anisotropic structure of the North American upper mantle from inversion of surface waveform data, *Geophys. J. Int.*, *171*(1), 206–222, doi:10.1111/j.1365-246X.2007.03465.x.

Masters, G., M. P. Barmine, and S. Kientz (2007), Mineos user's manual, in *Computational Infrastructure for Geodynamics*, Calif. Inst. of Technol., Pasadena.

McCarthy, J., and G. A. Thompson (1988), Seismic imaging of extended crust with emphasis on the western United States, *Geol. Soc. Am. Bull.*, *100*(9), 1361–1374, doi:10.1130/0016-7606(1988)100<1361:SIOECW>2.3.CO;2.

Moschetti, M. P., M. H. Ritzwoller, and N. M. Shapiro (2007), Surface wave tomography of the western United States from ambient seismic noise: Rayleigh wave group velocity maps, *Geochem. Geophys. Geosyst.*, *8*, Q08010, doi:10.1029/2007GC001655.

Moschetti, M. P., M. H. Ritzwoller, F.-C. Lin, and Y. Yang (2010), Seismic evidence for widespread western-US deep-crustal deformation caused by extension, *Nature*, *464*, 885–889, doi:10.1038/nature08951.

Nettles, M., and A. M. Dziewonski (2008), Radially anisotropic shear velocity structure of the upper mantle globally and beneath North America, *J. Geophys. Res.*, *113*, B02303, doi:10.1029/2006JB004819.

NGDC (2009), *Marine Trackline Geophysics*, Natl. Geophys. Data Center, NESDIS, NOAA. (http://map.ngdc.noaa.gov/website/mgg/trackline/viewer.htm)

Panning, M., and B. Romanowicz (2006), A three dimensional radially anisotropic model of shear velocity in the whole mantle, *Geophys. J. Int.*, *167*, 361–379, doi:10.1111/j.1365-246X.2006.03100.x.

Peng, X., and E. D. Humphreys (1998), Crustal velocity structure across the eastern Snake River Plain and Yellowstone swell, *J. Geophys. Res.*, *103*(B4), 7171–7186, doi:10.1029/97JB03615.

Pierce, K. L., and W. J. Morgan (1989), The track of the Yellowstone hotspot: Volcanism, faulting, and uplift, in *Regional Geology of Eastern Idaho and Western Wyoming*, edited by P. Link, M. Kuntz, and L. Platt, Mem. Geol. Soc. Am., 179, 1–53.

Pollitz, F. F. (2008), Observations and interpretation of fundamental mode Rayleigh wavefields recorded by the Transportable Array (USArray), *Geophys. J. Int.*, *173*, 189–204, doi:10.1111/j.1365-246X.2007.03666.x.

Potter, C. J., et al. (1987), Crustal structure of north-central Nevada; results from COCORP deep seismic profiling, *Geol. Soc. Am. Bull.*, *98*(3), 330–337, doi:10.1130/0016-7606(1987)98<330:CSONNR>2.0.CO;2.

Ramachandran, K., R. D. Hyndman, and T. M. Brocher (2006), Regional P wave velocity structure of the northern Cascadia subduction zone, *J. Geophys. Res.*, *111*, B12301, doi:10.1029/2005JB004108.

Roth, J. B., M. J. Fouch, D. E. James, and R. W. Carlson (2008), Three-dimensional seismic velocity structure of the northwestern United States, *Geophys. Res. Lett.*, *35*, L15304, doi:10.1029/2008GL034669.

Sabra, K. G., P. Gerstoft, P. Roux, W. A. Kuperman, and M. C. Fehler (2005), Extracting time-domain Green's function estimates from ambient seismic noise, *Geophys. Res. Lett.*, *32*, L03310, doi:10.1029/2004GL021862.

Saleeby, J. B., and C. Busby-Spera (1992), Early Mesozoic tectonic evolution of the western U.S. Cordillera, in *The Geology of North America*, vol. G3, *The Cordilleran Orogen: Conterminous US*, edited by B. C. Burchfiel, P. Lipman, and M. Zoback, pp. 107–168, Geol. Soc. of Am., Boulder, Colo.

Sambridge, M. (1999), Geophysical inversion with a neighbourhood algorithm-I. Searching a parameter space, *Geophys. J. Int.*, *138*(2), 479–494, doi:10.1046/j.1365-246X.1999.00876.x.

Shapiro, N. M., and M. Campillo (2004), Emergence of broadband Rayleigh waves from correlations of the ambient seismic noise, *Geophys. Res. Lett.*, *31*, L07614, doi:10.1029/2004GL019491.

Shapiro, N. M., and M. H. Ritzwoller (2002), Monte-Carlo inversion for a global shear-velocity model of the crust and upper mantle, *Geophys. J. Int.*, *151*(1), 88–105, doi:10.1046/j.1365-246X.2002.01742.x.

Shapiro, N. M., M. Campillo, L. Stehly, and M. H. Ritzwoller (2005), High resolution surface wave tomography from ambient seismic noise, *Science*, *307*(5715), 1615–1618, doi:10.1126/science.1108339.

Smith, R. B., and L. W. Braile (1994), The Yellowstone hotspot, *J. Volcanol. Geotherm. Res.*, *61*(3–4), 121–187, doi:10.1016/0377-0273(94)90002-7.

Snieder, R. K. (2004), Extracting the Green's function from the correlation of coda waves: A derivation based on stationary phase, *Phys. Rev. E*, *69*(4), 046610, doi:10.1103/PhysRevE.69.046610.

Stachnik, J. C., K. Dueker, D. L. Schutt, and H. Yuan (2008), Imaging Yellowstone plume-lithosphere interactions from inversion of ballistic and diffusive Rayleigh wave dispersion and crustal thickness data, *Geochem. Geophys. Geosyst.*, *9*(6), Q06004, doi:10.1029/2008GC001992.

Stehly, L., B. Fry, M. Campillo, N. M. Shapiro, J. Guilbert, L. Boschi, and D. Giardini (2009), Tomography of the Alpine region from observations of seismic ambient noise, *Geophys. J. Int.*, *178*(1), 338–350, doi:10.1111/j.1365-246X.2009.04132.x.

Tanimoto, T., and K. P. Sheldrake (2002), Three-dimensional S-wave velocity structure in southern California, *Geophys. Res. Lett.*, *29*(8), 1223, doi:10.1029/2001GL013486.

Thatcher, W., G. R. Foulger, B. R. Julian, J. Svarc, E. Quilty, and G. W. Bawden (1999), Present-day deformation across the basin and range province, Western United States, *Science*, *283*(5408), 1714–1718, doi:10.1126/science.283.5408.1714.

Tolan, T. L., S. P. Reidel, M. H. Beeson, J. L. Anderson, K. R. Fecht, and D. A. Swanson (1989), Revisions to the estimates of the areal extent and volume of the Columbia River Basalt Group, in *Volcanism and Tectonism in the Columbia River Flood Basalt Province*, edited by S. P. Reidel and P. R. Hooper, *Spec. Pap. Geol. Soc. Am.*, *239*, 1–20.

van der Lee, S., and A. Frederiksen (2005), Surface wave tomography applied to the North American upper mantle, *Geophys. Monogr.*, *157*, 67–80.

Villaseñor, A., Y. Yang, M. H. Ritzwoller, and J. Gallart (2007), Ambient noise surface wave tomography of the Iberian Peninsula: Implications for shallow seismic structure, *Geophys. Res. Lett.*, *34*, L11304, doi:10.1029/2007GL030164.

Wapenaar, K. (2004), Retrieving the elastodynamic Green's function of an arbitrary inhomogeneous medium by cross correlation, *Phys. Rev. Lett.*, *93*(25), 254301, doi:10.1103/PhysRevLett.93.254301.

Warren, L. M., J. A. Snoke, and D. E. James (2008), S-wave velocity structure beneath the High Lava Plains, Oregon, from Rayleigh-wave dispersion inversion, *Earth Planet. Sci. Lett.*, *274*(1–2), 121–131, doi:10.1016/j.epsl.2008.07.014.

Weaver, R. L., and O. I. Lobkis (2001), Ultrasonics without a source: Thermal fluctuation correlations at MHz frequencies, *Phys. Rev. Lett.*, *87*(13), 134301, doi:10.1103/PhysRevLett.87.134301.

Wernicke, B. (1992), Cenozoic extensional tectonics of the u.s. cordillera, in *The Geology of North America*, vol. G3, *The Cordilleran Orogen: Conterminous US*, edited by B. C. Burchfiel, P. Lipman, and M. Zoback, pp. 533–581, Geol. Soc. of Am., Boulder, Colo.

West, J. D., M. J. Fouch, J. B. Roth, and L. T. Elkins-Tanton (2009), Vertical mantle flow associated with a lithospheric drip beneath the Great Basin, *Nat. Geosci.*, *2*, 439–444, doi:10.1038/ngeo526.

Xue, M., and R. Allen (2006), Origin of the Newberry Hotspot Track: Evidence from shear wave splitting, *Earth Planet. Sci. Lett.*, *244*, 315–322, doi:10.1016/j.epsl.2006.01.066.

Yan, Z., and R. W. Clayton (2007), Regional mapping of the crustal structure in southern California from receiver function, *J. Geophys. Res.*, *112*, B05311, doi:10.1029/2006JB004622.

Yang, Y., M. H. Ritzwoller, A. L. Levshin, and N. M. Shapiro (2007), Ambient noise Rayleigh wave tomography across Europe, *Geophys. J. Int.*, *168*(1), 259–274, doi:10.1111/j.1365-246X.2006.03203.x.

Yang, Y., A. Li, and M. H. Ritzwoller (2008a), Crustal and uppermost mantle structure in southern Africa revealed from ambient noise and teleseismic tomography, *Geophys. J. Int.*, *174*(1), 235–248, doi:10.1111/j.1365-246X.2008.03779.x.

Yang, Y., M. H. Ritzwoller, F.-C. Lin, M. P. Moschetti, and N. M. Shapiro (2008b), Structure of the crust and uppermost mantle beneath the western United States revealed by ambient noise and earthquake tomography, *J. Geophys. Res.*, *113*, B12310, doi:10.1029/2008JB005833.

Yao, H., R. D. V. der Hilst, and M. V. de Hoop (2006), Surface-wave array tomography in SE Tibet from ambient seismic noise and two-station analysis: I. Phase velocity maps, *Geophys. J. Int.*, *166*, 732–744, doi:10.1111/j.1365-246X.2006.03028.x.

Yao, H., C. Beghein, and R. D. van der Hilst (2008), Surface-wave array tomography in SE Tibet from ambient seismic noise and two-station analysis: II. Crustal and upper mantle structure, *Geophys. J. Int.*, *173*, 205–219, doi:10.1111/j.1365-246X.2007.03696.x.

Zandt, G., S. C. Myers, and T. C. Wallace (1995), Crust and mantle structure across the Basin and Range-Colorado Plateau boundary at 37°N latitude and implications for Cenozoic extensional mechanism, *J. Geophys. Res.*, *100*(B6), 10,529–10,548, doi:10.1029/94JB03063.

Zheng, S. H., X. L. Sun, X. D. Song, Y. Yang, and M. H. Ritzwoller (2008), Surface wave tomography of China from ambient seismic noise correlation, *Geochem. Geophys. Geosyst.*, *9*, Q05020, doi:10.1029/2008GC001981.

F.-C. Lin, M. H. Ritzwoller, and Y. Yang, Center for Imaging the Earth's Interior, Department of Physics, University of Colorado, 390 UCB, Boulder, CO 80309-0390, USA. (fan-chi.lin@colorado.edu; michael.ritzwoller@colorado.edu; yingjie.yang@colorado.edu)

M. P. Moschetti, Geologic Hazards Science Center, USGS Denver Federal Center, PO Box 25046 MS 966, Golden, CO 80225, USA. (mmoschetti@usgs.gov)